

**AUTOMATION OF A DXA-BASED FINITE-ELEMENT TOOL FOR  
CLINICAL ASSESSMENT OF HIP FRACTURE RISK**

**By**

**Sharif Ahmed**

**A Thesis Submitted to the Faculty of Graduate Studies of**

**The University of Manitoba**

**In partial fulfillment of the requirements of the degree of**

**MASTER OF SCIENCE**

**Department of Mechanical Engineering**

**University of Manitoba**

**Winnipeg, Manitoba**

**Copyright © 2016 by Sharif Ahmed**

## Abstract

Dual Energy X-ray Absorptiometry (DXA)-based finite element (FE) modelling has emerged as a potential tool for better assessment of osteoporotic hip fracture risk. Automation of this complex and computationally-intense procedure is the prime requirement for its clinical applicability. The aim of this study was to develop a fully automatic DXA-based finite element tool and assess its discrimination ability and short-term repeatability. The proximal femur was automatically segmented from clinical hip DXA scan and the subject-specific FE model was constructed for simulating sideways fall. Hip fracture risk indices (HFRI) were calculated using two ways (along a femur cross-section and over a region of interest, ROI). Hip fracture discriminability increased when moved from femur cross-section based to ROI based HFRI calculation. A significant increase in hip fracture discriminability from baseline femoral neck and total hip bone mineral density (BMD) was achieved with ROI based HFRI. Promising short-term repeatability was observed for HFRI (coefficient of variation, CV, 3~3.5%). After removing representative poor cases, CVs were less than 3%. These preliminary results establish the potential of the proposed automatic tool for hip fracture risk assessment and justify large-scale clinical evaluation of its ability to predict incident hip fractures.

# Acknowledgments

I would like to express my heartiest gratitude to my advisor, Dr. Yunhua Luo for his full support, expert guidance, immense inspiration and assistance in my research and non-academic affairs as well. I would also like to express my immense appreciation to Dr. William D. Leslie and Dr. Shuman Yang for providing clinical cases to clinically validate the developed finite element procedure.

I gratefully acknowledge the partial support provided by the Manitoba Health Research Council (MHRC).

I am thankful to my colleagues Dr. Tanvir Rahman Faisal, Dr. Masoud Nasiri Sarvi, Mr. Hossain Kheirollahi and Ms. Huijuan Yang for all the academic discussions and happy working time. I also thank all my friends here in Winnipeg and back in my country for their consistent help and support.

Lastly, I want to thank my parents, my siblings and my spouse for their enormous affection and support.

# Dedication

To my parents.

# Contents

## Front Matter

|   |           |
|---|-----------|
| Contents.....   | iii       |
| List of Tables .....  | vi        |
| List of Figures .....   | vii       |
| List of Abbreviations.....  | ix        |
| List of Symbols .....   | x         |
| <b>1 Introduction</b>   | <b>1</b>  |
| 1.1 Motivation and background.....  | 1         |
| 1.2 Objective of the reported research .....  | 5         |
| 1.3 Outline of the reported research .....  | 5         |
| <b>2 Literature reviewing of Image-based finite element models</b>                                  | <b>8</b>  |
| 2.1 Theoretical advantages of FEA over statistical models.....                                      | 8         |
| 2.2 Previous QCT and DXA-based finite element models for assessing osteoporotic fracture risk.....  | 12        |
| 2.3 Knowledge gap in previous research .....  | 21        |
| <b>3 Automation of DXA-based finite element modelling procedure for assessing hip fracture risk</b> | <b>22</b> |
| 3.1 DXA-based finite element modelling .....  | 22        |
| 3.2 DXA-image .....   | 24        |
| 3.3 Automatic segmentation and generation of finite element mesh .....                              | 25        |
| 3.4 Automatic detection of critical femur cross-sections and Regions of Interest (ROIs) .....       | 26        |
| 3.4.1 Detection of critical femur cross-sections .....  | 27        |

|          |  |           |
|----------|--|-----------|
| 3.4.2    | Detection of Regions of Interest (ROIs) .....  | 28        |
| 3.5      | Material models .....  | 29        |
| 3.6      | Plane stress model with triangular elements .....  | 33        |
| 3.7      | Loading and boundary condition simulating a sideways fall .....  | 36        |
| <b>4</b> | <b>Calculation of hip fracture risk indices</b>  | <b>38</b> |
| 4.1      | Hip fracture risk indices .....  | 38        |
| 4.1.1    | HFRI at critical femur cross-section .....   | 39        |
| 4.1.2    | HFRI at Region of interest (ROI) .....   | 40        |
| <b>5</b> | <b>Clinical studies</b>  | <b>42</b> |
| 5.1      | Short-term repeatability .....   | 42        |
| 5.2      | Discrimination ability in a small-scale retrospective clinical study ..  | 44        |
| 5.3      | Clinical cases extracted from Manitoba Bone Mineral Density Database for the studies .....                                   | 46        |
| <b>6</b> | <b>Results</b>   | <b>47</b> |
| 6.1      | AUCs for different material models .....   | 48        |
| 6.2      | AUCs at critical femur cross-sections, self-defined & clinical Regions of Interest (ROIs) for identical material model ..... | 51        |
| 6.3      | Correlation analysis .....   | 53        |
| 6.4      | Short-term repeatability of HFRI's .....   | 54        |
| <b>7</b> | <b>Discussion</b>  | <b>57</b> |
| 7.1      | Assessment of hip fracture discriminability of HFRI's .....  | 57        |
| 7.1.1    | AUCs for different martial models .....  | 57        |
| 7.1.2    | AUCs at critical femur cross-sections .....  | 60        |
| 7.1.3    | AUCs at self-defined ROIs .....  | 63        |
| 7.1.4    | AUCs at clinical ROIs .....  | 65        |
| 7.2      | Assessment of correlation analysis .....   | 68        |

|                    |  |           |
|--------------------|--|-----------|
| 7.3                | Assessment of short-term repeatability results ..... | 69        |
| <b>8</b>           | <b>Conclusions and future work</b>                   | <b>74</b> |
| 8.1                | Conclusions and contributions .....                  | 75        |
| 8.2                | Limitations of the present study .....               | 77        |
| 8.3                | Future work.....                                     | 79        |
| <b>Back Matter</b> |  | <b>81</b> |
|                    | Bibliography .....                                   | 81        |

# List of Tables

|  |    |
|--|----|
| Table 1: Demographic information for the 390 clinical cases .....  | 46 |
| Table 2: AUCs (95% CI) for HFRIIs when yield stress was derived from Young’s modulus<br>.....                | 49 |
| Table 3: AUCs (95% CI) for HFRIIs when yield stress was derived from BMD .....                               | 50 |
| Table 4: AUCs (95% CI) for HFRIIs calculated with different approaches but identical<br>material model ..... | 52 |
| Table 5: CVs (%) for HFRIIs at clinical ROIs.....  | 55 |
| Table 6: CVs (%) for areal BMDs at clinical ROIs .....   | 55 |

# List of Figures

|  |    |
|--|----|
| Figure 1: The methodology to calculate hip fracture risk indices using automatic DXA-based FE method and assess hip fracture discriminability .....  | 23 |
| Figure 2: A sample DXA image .....   | 24 |
| Figure 3: Regions of Interest (ROIs) defined by the DXA scanner.....   | 25 |
| Figure 4: Step-by-step procedure to segment proximal femur and mesh generation, (a) Hip-shaft outline (b) Shaft outline (c) Circle fitted inside head ROI (d) Segmented femur (e) Meshed femur ..... | 26 |
| Figure 5: Critical cross-sections at proximal femur.....   | 27 |
| Figure 6: (a) Self-defined (10mm wide) and (b) Clinical regions of interest .....  | 28 |
| Figure 7: Convergence test at clinical trochanteric ROI.....   | 33 |
| Figure 8: A typical sideways fall .....  | 37 |
| Figure 9: Loading and boundary condition simulating a sideways fall .....  | 37 |
| Figure 10: A sample ROC curve.....   | 45 |
| Figure 11: AUCs at clinical ROIs when yield stress was derived from Young's modulus .....  | 48 |
| Figure 12: AUCs at clinical ROIs when Yield stress was derived from BMD .....  | 50 |
| Figure 13: AUCs for HFRI calculated at femur cross-sections, self-defined and clinical ROIs when identical material model was used in FE analysis .....  | 52 |
| Figure 14: Correlation between HFRI and in-house BMD at clinical (a) Femoral neck (b) Trochanter (c) Shaft and (d) Total ROI .....   | 53 |

|   |    |
|---|----|
| Figure 15: Correlation between in-house and true areal BMD at clinical femoral neck ROI<br>.....  | 54 |
| Figure 16: Mean and standard deviation of HFRI at clinical ROIs.....  | 54 |
| Figure 17: Ten representative cases responsible for poor repeatability in HFRI.....   | 56 |
| Figure 18: Effect of femur rotation on position of femur cross-sections.....  | 61 |
| Figure 19: Positioning of subtrochanteric cross-section close to distal boundary.....   | 62 |
| Figure 20: Effect of femur rotation on placement of self-defined ROIs.....  | 64 |
| Figure 21: Position of subtrochanteric ROI in a short femur.....  | 65 |
| Figure 22: Relative positions of clinical and self-defined femoral neck ROI and linearly<br>interpolated portion in segmented contour ..... | 66 |
| Figure 23: Relative positions of self-defined subtrochanteric ROI and clinical shaft ROI<br>while scan length was (a) normal (b) short..... | 67 |

# List of Abbreviations

|                                    |       |
|------------------------------------|-------|
| Area Under the Curve               | AUC   |
| Body Mass Index                    | BMI   |
| Bone Mineral Density               | BMD   |
| Coefficient of Variation           | CV    |
| Confidence Interval                | CI    |
| Dual-energy X-ray Absorptiometry   | DXA   |
| Femoral Neck                       | FN    |
| Finite Element                     | FE    |
| Hip Fracture Risk Index            | HFRI  |
| Hip Structure Analysis             | HSA   |
| Intertrochanter                    | IT    |
| Quantitative Computed Tomography   | QCT   |
| Receiver Operating Characteristics | ROC   |
| Region of Interest                 | ROI   |
| Subtrochanter                      | SUB   |
| Three-dimensional                  | 3D    |
| Trochanter                         | Troch |
| Two-dimensional                    | 2D    |
| Volumetric Bone Mineral Density    | vBMD  |

# List of Symbols

|                               |                                  |                          |             |
|-------------------------------|----------------------------------|--------------------------|-------------|
| Approximated displacement     | $\tilde{\mathbf{u}}^{(e)}$       | Sample size              | N           |
| Area of triangle              | $\Delta$                         | Shear stress             | $\tau_{xy}$ |
| Ash Density                   | $\rho_{\text{ash}}$              | Statistical significance | $p$         |
| Co-efficient of correlation   | R                                | Stress in x-direction    | $\sigma_x$  |
| Deformation matrix            | B                                | Stress in y-direction    | $\sigma_y$  |
| Effective stress              | $\sigma_{\text{eff}}$            | Thickness                | t           |
| Element force vector          | $\mathbf{f}^{(e)}$               | Width                    | W           |
| Element shape function matrix | $\mathbf{N}^{(e)}$               | Yield strength           | $\sigma_Y$  |
| Element stiffness matrix      | $\mathbf{k}^{(e)}$               | Yield Stress             | Y           |
| Element strain                | $\boldsymbol{\varepsilon}^{(e)}$ | Young's Modulus          | E           |
| Element stress                | $\boldsymbol{\sigma}^{(e)}$      |                          |             |
| Global force vector           | F                                |                          |             |
| Global stiffness matrix       | K                                |                          |             |
| Material property matrix      | D                                |                          |             |
| Nodal displacements           | $\mathbf{U}^{(e)}$               |                          |             |
| Poisson's ratio               | $\nu$                            |                          |             |

# Chapter 1

## Introduction

### 1.1 Motivation and background

Osteoporosis is a global health concern that will escalate with the growing and aging world population [1]. The distinctive characteristics of this disease is low bone mass with altered skeletal structure and strength that jointly contribute to fracture susceptibility, resulting in severe disability, morbidity, and even mortality [1-3]. Hip, spine, and distal forearm are typical sites for osteoporotic fracture [1]. In 2000, among 9.0 million global osteoporotic fractures, there were 1.6 million hip fractures, 1.4 million spine fracture and 1.7 million forearm fractures [4]. The count of hip fractures is estimated to exceed 3.94 million in 2025 and 6.2 million by the year 2050 [5]. In 2005, hip fracture constituted 14% of all incident fractures in the United States and 72% of direct economic costs [6]. In Canada, approximately 24,000 hip fracture occurred in 1993-1994 and estimated to be quadrupled by 2041 [7]. As a direct consequence, hip fracture related annual healthcare cost is expected to raise from \$650 million in 1995-1996 to \$2.4 billion by the year 2041 [8]. The accurate

detection of those at high risk of fracture permits appropriate targeted preventive interventions. Consequently, effective patient management will be possible and annual healthcare cost will be diminished. Therefore, significant efforts by researchers have been devoted towards developing techniques for accurate assessment of osteoporotic fracture risk.

Routine clinical care requires an accurate, safe, cost-effective and non-invasive method for osteoporotic fracture risk assessment. Currently, dual energy X-ray absorptiometry (DXA) defined areal (projected) bone mineral density (BMD) is used as a reference criterion for screening osteoporosis and recognizing patients with greater risk of fracture [9]. However, its ability to assess patient-specific fracture risk is limited because a large number of osteoporotic fractures happen in patients having BMD higher than the standard distinctive threshold for osteoporosis (BMD T-score  $\leq -2.5$ ) [10-12]. Variability in bone mineral density can explain less than fifty percent (<50%) variation in bone strength [13-16]. It suggests that BMD cannot be the sole parameter that defines bone strength. Distinct clinical and biomechanical risk factors such as individual age, body mass index, fall dynamics, bone quality and bone geometry also contribute to bone strength [17-21].

Several efforts have been directed towards considering more risk factors while assessing individual hip fracture risk. The fracture risk assessment tool (FRAX) considers BMD as well as clinical risk factors to evaluate chances for ten-year major osteoporotic fractures [21]. The FRAX is developed from population-based cohorts and inapplicable in all geographic areas. Moreover, it does not consider subject-specific biomechanical risk factors such as impact force from accidental falls and femur geometric parameters when evaluating fracture risk. Therefore, this tool is more suitable for statistical analysis in large

populations and possesses limited applicability in subject level. The hip structure analysis (HSA) utilizes BMD and bone geometry information to estimate parameters associated with bone strength and hip fracture risk [22-27]. Two-dimensional structural engineering models such as curved beam [28] and curved composite beam [29] model have been developed to integrate impact force with density and geometry information. Femur strength information derived from those models is a significant discriminator of hip fracture [26, 27, 30, 31]. However, HSA parameters and/or derived strength data did not outperform or significantly improve hip fracture discrimination capability when compared with BMD alone [26, 27, 32]. Complicated deformation pattern at the femoral neck and intertrochanteric region, together with underlying assumptions of the beam model could be responsible for this deficiency [33]. Therefore, finite element (FE) modelling has emerged as an alternative approach to estimate hip strength.

Medical image-based FE modelling combines radiographic information with biomechanics to consider relevant factors leading to hip fracture. Several studies have shown that FE modelling is a promising tool to assess patient-specific hip fracture risk [17, 33-39]. Three-dimensional (3D) and two-dimensional (2D) FE model can be constructed from quantitative computed tomography (QCT) and DXA, respectively. Although 3D FE analysis (FEA) predicts femoral strength with high accuracy [35, 40, 41], high cost and exposure to high ionizing radiation currently limits its role to research [42]. Conversely, noteworthy progress has recently been achieved in predicting femoral fracture load using the DXA-based FE method [38, 39]. In terms of discriminating hip fractures evaluated by the area under the receiver-operating-characteristic curve, abbreviated as AUC (details will be discussed in section 5.3), parameters derived from DXA-based finite element models

perform better than BMD alone [27, 38]. Therefore, computational efficiency and improved discrimination ability make DXA-based FE model a strong candidate for hip fracture risk assessment in the clinical settings. In addition, low radiation dosage and widespread availability together with low installation cost have established DXA as the primary imaging modality for the present and foreseeable future.

Site specific hip fracture risk index (HFRI) calculated from DXA-based FE model has been proposed for hip fracture risk assessment [33, 37]. HFRI is a measure of likelihood of fracture at the corresponding site. It has been calculated at critical cross-sections and over regions of proximal femur described as regions of interest or ROIs (see Figure 5, Figure 6 and Chapter 4 for details). However, HFRI were not clinically assessed for hip fracture discrimination accuracy. For clinical applicability, HFRI must have higher hip fracture discrimination accuracy than the current level for BMDs. Additionally, high reproducibility of the HFRI is required to detect a small change in bone quality.

Prior to clinical application, a robust and reproducible method should be capable of processing cases with minimal human intervention. Current techniques of DXA-based FE model generation involves manual segmentation of proximal femur followed by mesh generation, material property assignment and solving finite element equations. Manual segmentation was identified as a significant source of variability [37]. Additionally, a manual process is costly, tedious and laborious, hence, unsuitable for clinical application. Consequently, a fully automatic DXA-based FE model might pave the way for clinical assessment of hip fracture risk. Finite element results are largely affected by the empirical equations used to estimate bone material properties during finite element modelling. A

good material model will aid proper estimation of bone material properties and hence improve performance of HFRIIs derived from the DXA-based FE model.

## 1.2 Objective of the reported research

The main objective of this thesis is to develop a fully automatic subject-specific DXA-based finite element (FE) tool for clinical assessment of hip fracture risk. To improve hip fracture discrimination accuracy, different material models will be tested in the automatic FE tool. With the best material model, different approaches of HFRI calculation will be contrasted and the effect of ROI definition on the hip fracture discrimination accuracy of automatic tool derived HFRIIs will be analyzed. Short-term repeatability of indices will be calculated to assess their reproducibility. An accurate and precise tool will enable clinical identification of more patients at hip fracture risk. Consequently, determination of patient-specific targeted treatment and monitoring the effect of a drug will be more accurate and easier.

## 1.3 Outline of the reported research

The thesis is organized in the following manner:

**Chapter 2** – In this chapter, theoretical advantages of finite element models over traditional statistical models of fracture risk assessment will be reviewed. Additionally, previous finite element models developed from medical images will be reviewed along with their respective advantages and limitations.

**Chapter 3** – In this chapter, the process of automatizing DXA-based finite element method will be described. The proximal femur will be segmented from hip automatically and all parameters associated with finite element model construction will be assigned automatically to the model. Finite element mesh size will be selected based on convergence study. Different material models selected for testing in the finite element model will be introduced. The methodology to automatically detect different femur cross-sections and two types of regions of interest will also be presented.

**Chapter 4** – In this chapter, two techniques of hip fracture risk index calculation i.e. along a femur cross-section and over an ROI will be introduced followed by the process of calculating hip fracture risk indices using those approaches.

**Chapter 5** – In this chapter, theoretical background of assessing discriminability (accuracy) and repeatability (precision) of a diagnostic variable will be discussed. Statistical characteristics of the studied cases will also be reported.

**Chapter 6** – In this chapter, area under the receiver-operating-characteristics curve (AUC) values of automatic FE tool derived hip fracture risk indices (HFRI) will be reported. At first, AUCs obtained from different material models will be reported. Then, AUCs of HFRI calculated with two techniques will be compared. AUCs for two types of ROIs such as self-defined and clinical will also be contrasted. Next, correlation between HFRI and densitometric measures will be reported. Finally, reproducibility of the HFRI will be covered.

**Chapter 7** – In this chapter, relevant findings associated with obtained results will be discussed. Possible reasons behind improvement or deterioration in the performance of HFRI will be analyzed.

**Chapter 8** – This chapter will include major conclusions, contributions, and limitations.

Future research will be directed to deal with the limitations and explore possibilities of potential applications.

## Chapter 2

# Literature reviewing of Image-based finite element models

### 2.1 Theoretical advantages of FEA over statistical models

Osteoporosis is a kind of skeletal disease distinguished by thin bone, increased bone frailty and fracture risk [43]. A progressive and continuous increase in fracture risk was observed with decreasing bone mineral density [44-49]. Total bone mass present in a unit volume ( $\text{g}/\text{cm}^3$ ) or area ( $\text{g}/\text{cm}^2$ ) of bone is the bone mineral density and it is quantified by densitometric techniques. The most recognized technique is to measure areal bone mineral density ( $\text{g}/\text{cm}^2$ ) by dual-energy X-ray absorptiometry (DXA) as X-ray absorption is highly responsive to Calcium [9] which is the primary element of bone tissue. Bone density measurement has high specificity in assessing fracture risk [50], therefore, a threshold value for bone mineral density was needed to identify high-risk patients from others. Several population-based approaches were adopted to define an appropriate cutoff value.

In one approach, it was set equal to the average BMD of the reference population with identical age, gender, and height as of the studied patient (Z-score) [51]. The subject's BMD is juxtaposed with the threshold value to approximate the relative risk of fracture. The major pitfall of using age-matched reference group is that the fracture risk will become independent of age [52]. Instead, the cutoff could be set somewhere lower than average BMD of young adults [53]. To satisfy most of the statistical criteria, the cut off value was set at 2.5 times standard deviation below the average BMD of young and healthy adults [52]. The areal bone mineral density is converted into an equivalent T-score and relative level of osteoporosis is measured. A patient with T-score lower than -2.5 ( $T\text{-score} < -2.5$ ) is recognized to have severe osteoporosis and at higher risk of fracture. An obvious limitation is associated with foregoing statistical models. An overlap exists between bone mineral density distribution for fractured and non-fractured patients in the population [52]. Bone density measurement has high specificity and low sensitivity in respect of fracture prediction [54, 55]. As a consequence, many fractures occur with patients recognized as low-risk patients based on their normal bone mineral density. Therefore, although bone density measurement can predict relative risk level but unable to distinguish patients who will have a fracture [9, 10].

Apart from bone mineral density, clinical factors are also responsible for fragility fractures. Between the age of 50 and 80, hip fracture incident increases 10 folds more with age than BMD [9, 56]. Additional risk factors for example body mass index (BMI), parental history, and alcohol intake give information on fracture risk [54, 57, 58]. Combining clinical risk factors with BMD resulted in higher sensitivity and specificity than unaccompanied [59]. Therefore, clinical risk factors and bone mineral densities were integrated into a single tool

to predict hip fracture risk. Fracture risk assessment tool (FRAX) was introduced in 2008 to predict individual 10-years hip fracture probability [21]. The associations between risk factors and fracture risk were established based on validated population-based cohort data [59]. Since FRAX utilizes average population characteristics to predict individual hip fracture risk, it may provide incorrect prediction especially when an individual has risk factors other than those included in the FRAX tool such as presence of diabetic. In other words, absolute condition of an individual may not be well explained by statistical models. FRAX can only be used in participating countries where both fracture and mortality information is available. It cannot be used worldwide because fracture probability is highly dependent on geographic location [60]. Country-specific fracture rate changes over time [61]. Therefore, population database needs periodical updates which will be laborious and expensive. In addition, in the absence of an intervention threshold for FRAX model, determining one will be expensive [59]. There are other limitations associated with FRAX model, for example, omission of important risk variables such as risk of fall, bone geometry, ignoring cross-country geographic variation etc. [62, 63]

Low trauma causing falls for example a fall from standing height is responsible for approximately 90% of hip fractures [64]. Sideways falls accompanied by reduced bone mass from osteoporosis could be the most critical condition to cause a hip fracture in elderly people [65, 66]. Unfortunately fall-related biomechanical factors such as the risk of fall, impact force have been omitted in the statistical methods of fracture prediction. Therefore, biomechanical models constructed from medical images are attracting much attention in recent years. Biomechanical models utilize bone density, geometry and impact force information to assess individual fracture risk. Structural engineering model such as

two-dimensional beam models have been developed from DXA-images [28, 29] for femur strength assessment, however, they have limited applicability because of their poor performance arising from inherent assumptions and complicated deformation pattern of proximal femur [26, 33]. On the other hand, finite element method is a popular tool for engineering analysis of structures and has been successfully implemented in many branches of engineering. Finite element model of bone inherently depends on bone mineral density, bone geometry, and impact force. Those models are capable of capturing point-to-point variation in material properties, hence precise deformation patterns caused by external forces can be obtained [36]. Finite element derived parameters were found to be more sensitive to alteration in trabecular bone density and femur geometry than areal bone mineral density [67]. It implies FE analysis of the proximal femur can explain more variability in bone strength and may enhance strength prediction than with areal BMD. In fact, Cody et al. [40] contrasted between the ability of statistical and FE method in predicting femoral fracture load. The FE method was able to explain at least 20% more variability in femoral strength than the BMD. Age-related decay in FE-derived strength was higher than femoral neck BMD [68], which indicates more patients at higher risk of fracture can be recognized by FE-derived parameter than with the traditional BMD based osteoporosis classification system. Unlike statistical models, FE analysis is a deterministic tool that considers patient specific instead of population characteristics to assess individual hip fracture risk. Therefore, patient-specific FE analysis is more promising for individual hip fracture risk assessment. Although the construction of medical image-based FE model is still in the development stage, a properly constructed and validated finite element tool will outperform current method of individual hip fracture risk assessment.

## 2.2 Previous QCT and DXA-based finite element models for assessing osteoporotic fracture risk

A substantial amount of research has been devoted towards the development of a clinically applicable image-based patient-specific FE model for accurate assessment of hip fracture risk. Three-dimensional and two-dimensional FE model can be developed from QCT and DXA image respectively. Both three and two-dimensional FE analysis showed statistically equal sensitivity to a change in femur density and geometry [67]. In this section, relevant research and findings related to hip fracture risk assessment using three and two-dimensional FE analysis will be discussed. Relative advantages and limitations of three and two-dimensional FE analysis will also be addressed.

Lotz et al. [34, 69] pioneered the implementation of QCT based FE model in the investigation of hip fracture risk. In part-I [34], a linear FE model was constructed from QCT scans. Both cortical and trabecular bone was distinguished and modeled separately. Bone's inhomogeneous material properties were estimated from CT numbers. The material behavior was considered transversely isotropic and isotropic respectively for cortical and trabecular bone. Loading and boundary condition simulating one-legged stance and sideways fall was considered separately. Finite element derived strengths were validated against *in vitro* studies. The predicted onset of yielding was within 22 and 4 percent, and fracture load was within 8 and 5 percent of *in vitro* failure data, for stance and sideways fall respectively. In part-II [69], non-linear characteristic of trabecular and cortical bone was added in the model. Unlike part-I, isotropic material behavior was considered for both

type of bone. In this case, an improvement in yield prediction (within 2 and 1 percent of *in vitro* fracture data, respectively for stance and sideways fall) and a compromised improvement in predicted fracture load (within 1 and 17 percent of *in vitro* fracture data, respectively for stance and sideways fall) was observed. For sideways fall, the onset of yielding predicted by the linear model was close to that for the non-linear model. In contrast, predicted failure load had poor accuracy when the non-linear behavior was considered. Model preparation and execution time was higher for non-linear analysis. Therefore, the authors suggested using a linear finite element model to estimate bone strength. Irrespective of the type of FE model (linear or non-linear), fracture was predicted at the subcapital region for single-legged stance while at the trochanteric region for sideways fall. Since only two femurs were tested, so the results were statistically insignificant.

Keyak et al. endeavored series of analysis to build an accurate, clinically acceptable QCT based finite element tool. Before 1990, construction of three-dimensional FE model required significant time and engineering expertise of the user. Keyak et al. [70] proposed a novel methodology to automate three-dimensional FE modelling of the femur bone. Three-dimensional geometry of femur bone was recreated from contiguous CT scan slices using thresholding and edge-following algorithms. FE model was constructed with linear isotropic elements. The user could control the size of the finite elements. Apparent density was calculated from CT number and elastic modulus was estimated as a function of apparent density and constant strain rate. Elastic modulus was defined for each element as average Young's modulus of the pixels within the element. Forces from single limb

supported gait were applied quasi-statically through femoral head and greater trochanter. It was found that FE model produced stress fields were less uniform than those reported in the literature. Additionally, estimated stresses were discordant with the findings of Lotz et al. [71]. The authors attributed dissimilarity in loading condition and material properties assignment technique behind the discrepancy. In an attempt to improve model prediction, Keyak et al. [35] increased the number of different elastic modulus specified in the FE model from 50 to 170. The simulation was conducted for stance phase of gait and impact from a fall. The onset of local failure was assumed when fifteen contiguous elements had a factor of safety lower than unity ( $FOS < 1$ ). Fracture load was predicted from FEA and validated against *in vitro* destructive testing of the femur. FE predicted fracture load had a significant linear correlation with the measured fracture load for each loading condition ( $R=0.87$  and  $0.95$  for stance and fall respectively). Based on the 95% confidence interval reported, in identifying patients with below average fracture load, the linear FE model with fall configuration would correctly identify at least 14 times more patients than with stance configuration. Therefore, to identify more patients prone to spontaneous fracture, they proposed the construction of a non-linear FE model for stance configuration [72].

In 2001, Keyak et al. [73] validated the proposed QCT based FE model to assess its accuracy in identifying fracture location and type. Fracture location referred to the exact location of fracture while fracture type meant either cervical or trochanteric fracture. A semi-automatic linear FE model was generated from QCT image following the procedure developed earlier [35]. Both stance and fall loading condition were considered separately for the analysis. The location where 15 contiguous elements had the lowest factor of safety

(FOS) was identified as fracture onset location. In the experimental setup, a constant rate of displacement was applied on the cadaveric femora until failure. Radiographic image of the failed femur was captured and matched against the FE predicted fracture location. The accuracy of predicted fracture location was about 70% for both loading condition. The cervical fracture was predicted by stance loading condition with 72% accuracy and no trochanteric fracture was identified. In fall configuration, trochanteric and cervical fractures were identified with 79% accuracy. The onset of fracture locations identified here were in concordance with the previous study by Lotz et al. [34, 69]. Since the addition of non-linearity in the model improved the accuracy of predicted fracture load for stance configuration [72], therefore, a separate non-linear model was constructed to evaluate its accuracy in predicting fracture location [74]. Femoral strength was specified as the highest total reaction force at the head of the femur and it correlated well with experimental data. The model consistently identified fracture locations when at least some subcapital site was involved and failed to predict bicervical and intertrochanteric fractures. On the basis of evidence, it can be hypothesized that a non-linear FE model is more appropriate for spontaneous hip fracture and a linear FE model for fall induced hip fracture. Although Keyak et al. claimed an automatic FEA, the FEA was semi-automatic in actual. In fact, the FEA was automatic after the segmentation was completed. The difficulty was involved in separating the femoral head from soft tissue in CT scan data. Proper segmentation of femoral head from acetabulum was contingent upon CT scan resolution. In their studies reported here, Keyak et al. experimented 18 pairs of femur, therefore the outcomes were not statistically significant. Large-scale prospective or retrospective study (see Section 5.2

for details) was required to establish the superiority of QCT based finite element analysis in fracture prediction.

In a prospective case-cohort study, Orwoll et al. [41] analyzed the association between QCT based finite element measure of hip strength and hip fracture risk. A subject-specific semi-automatic non-linear FE model was constructed from QCT scan and asymmetry in tensile-compressive strength of bone was considered. The model was simulated for sideways fall and sideways impact load was calculated from patient height and body weight [75]. A uniform soft tissue thickness was considered for all subjects and a linear relation between soft tissue thickness and peak impact force was assumed. Hip strength was estimated from resulting non-linear force-deformation curve and load-to-strength ratio was estimated afterward. Cox proportional hazard regression and Prentice weighting method was adopted to model time to first hip fracture and Hazard Ratio (HR) was expressed as per 1 standard deviation change in the covariate such as femoral strength [76]. A strong connection was found between FE-derived parameters and hip fracture risk, so for areal BMD (unadjusted HR=13.1, 4.0 and 5.1 for femoral strength, load-to-strength-ratio and areal BMD respectively) [41]. However, after adjusting for age and areal BMD, hazard ratio for the load-to-strength ratio stayed statistically significant while femoral strength did not. In addition, the area under the ROC curve (AUC) values for FE-derived parameters were lower than the value for areal BMD (unadjusted AUC=0.83, 0.79 and 0.84 for femoral strength, load-to-strength-ratio, and total hip BMD respectively). Even after doing adjustments for age, body mass index and clinical center, AUCs of FE-derived parameters failed to exceed AUC for areal BMD (adjusted AUC=0.87, 0.88 and 0.88 respectively).

Although fracture predictability of FE-derived parameters and areal BMD was not significantly different, the authors argued the superiority of 3D FEA on the basis of its higher HR and sensitivity at high specificity. In essence, more research is required to evaluate the performance of QCT based FE method in a clinical environment.

Three-dimensional FE model generated from QCT image has the potential to accurately predict femoral strength [72, 77], however, clinical implementation of QCT based FEA is hard to achieve. Expensive computational device is required to solve 3D FE model within clinically acceptable time. Moreover, a robust segmentation and meshing technique is currently unavailable for 3D FEA. Additionally, CT scanning involves high radiation dosage for the patient, hence non-routinely used in clinics. On the contrary, DXA is the primary imaging modality in the clinics and exposes low radiation dosage. A two-dimensional image of the femur can be readily obtained and segmentation, meshing, FEA of 2D geometry is faster and more robust than QCT-based FEA [42]. Consequently, much attention has been devoted towards utilizing 2D images of the proximal femur for hip fracture risk assessment.

In order to retain the accuracy of 3D FEA while using 2D images, Langton et al. [42] proposed regeneration of 3D finite element model from 2D radiographs. The 2D radiographs were two-dimensional projected image of QCT scans. Using an average 3D shape template they reconstructed a 3D density distribution of 2D radiographs. Volumetric density was obtained by dividing areal BMD of pixels ( $\text{g}/\text{cm}^2$ ) by the 3D template derived bone depth. Subsequently, Young's modulus was estimated from volumetric density. The FE model was simulated for stance configuration and FE predicted femoral stiffness agreed

well to the experimental failure load. A major shortcoming of the proposed method was the usage of the average 3D template of the proximal femur constructed from CT scan of excised femora. To develop an accurate template, a large sample size is required which will be very expensive.

To avoid complexity associated with 3D FEA, Bujis et al. [36] assessed the feasibility of 2D finite element model to estimate femoral stiffness and strength. They developed a 2D FE model from an equivalent 2D image projected from CT scans. They computed element Young's modulus directly from element average (areal) bone mineral density. Identical loading and boundary condition was adopted in both FE simulation and experimental validation. Finite element derived strength and stiffness correlated well with experimental data. Moreover, FE-derived strain distribution mimicked experimental strain distribution. Although the work of Langton et al. [42] and Bujis et al. [36] addressed the relevance of using FE model constructed from 2D image to estimate the strength of a 3D geometry, however, these 2D images were reproduced from CT scan. Therefore, the issue of high radiation exposure could not be solved and true clinical performance of the proposed methods could not be assessed. Using equivalent 2D radiographs does not address the issues associated with segmenting proximal femur in a true 2D image. The proper approach could be developing a 2D FE model from standard radiograph or DXA image.

Testi et al. [17] constructed a 2D FE model specifically from DXA image for proximal femur strength assessment. The proximal femur was segmented from BMD file using thresholding and manual correction operations. The mesh was generated from contour coordinates. Element Young's modulus was estimated from average BMD of the element.

A linear relation between those two parameters was assumed. Instead of a subject specific impact force, the model was simulated with a constant sideways impact force. 2D FE results were validated *in vitro* by using an artificial femur and compare to 3D FEA results. 2D FE predicted principal strains were in close agreement with strains predicted by 3D FEA and within an acceptable range when compared to experimental results. FE predicted strain field mimicked the clinical strain distribution observed for sideways falls. Location of maximum strain was always at the femoral neck area. A retrospective study conducted on 93 Caucasian women revealed that adding FE-derived peak principal strain to bone mineral density significantly improved accuracy in classifying femoral neck fracture patients from non-fracture ones [78]. They proposed an index to estimate fracture risk of the femoral neck. The index was defined as a quotient of maximum FE-derived principal tensile strain and the ultimate strain directly derived from patient's age. However, hip fracture discriminability of the index was not assessed.

Thevenot et al. [79] analyzed the fracture discrimination accuracy of 2D FE model developed from standard radiographs (X-ray). When simulated for sideways fall, the FE model discriminated cervical and trochanteric hip fractures satisfactorily (79.6% and 85.7% respectively). The discrimination was made based on the location of maximum stress and path of continuous stress pattern within the trabecular bone. Trabecular and cortical bone was modeled separately, which cannot be attained in a DXA image. Subject specific material properties and loading condition was not implemented in the study. However, this study supports the hypothesis that a simple 2D FE model is capable of discriminating hip fractures alike complex 3D FE model. In a separate study, Pisharody et

al. [67] found statistically equivalent sensitivities of 2D and 3D FEA to a change in bone geometry and density.

Naylor et al. [38] determined the strength of the femur from DXA-based FE model and proposed a global fracture risk index namely load-to-strength ratio (LSR) to identify hip fracture cases from controls. The proximal femur was segmented from BMD map manually. The segmented femur was considered as a plate and a subject-specific uniform thickness was assumed for the plate. The areal BMDs were converted into volumetric BMDs and bone's inhomogeneous material properties were calculated from it. The FE model was simulated for sideways falls and femoral strength was defined as the impact force which stimulates maximum stress ratio in a contiguous area of 25 mm<sup>2</sup>. LSR was obtained by dividing the attenuated impact force by the estimated strength. FE-derived strength correlated well with the experimental strength. In terms of hip fracture discriminability, a modest increase from baseline femoral neck BMD was observed. Perhaps, a later study claimed DXA-based FE analysis as an independent predictor which had a significantly strong association with incident hip fracture compared to FRAX score [39].

For more accurate assessment of osteoporotic hip fracture risk and identify specific fracture location, Luo et al. [33] developed a DXA-based subject-specific FE model. Fracture risk was calculated at three critical cross-sections and defined as a ratio of stress induced by external force to the yield stress of the corresponding cross-section. Segmentation of the proximal femur was done manually and material properties were assigned directly from areal bone mineral density. An identical trend in the variation of the fracture risk indices

was observed alike areal BMD and T-score. Subsequently, Luo et al. [37] calculated hip fracture risk indices at 10mm wide regions of interest with a view to keeping consistency with the clinical method of BMD calculation and improve repeatability of the risk indices. They found clinically acceptable repeatability of the indices when high-quality cases were separated. However, hip fracture discrimination capability of the indices was not assessed.

## 2.3 Knowledge gap in previous research

It is clear from the literature review that image based FE method is a promising tool for hip fracture risk assessment. However, to be implemented in clinics, the tool should be automatic, inexpensive, harmless, fast and accurate. DXA-based FE analysis fulfills most of the criterion except automation. DXA-based FE models previously developed were semiautomatic. Therefore, the main objective of this study was to fully automate the DXA-based FE model. A retrospective study was conducted to determine hip fracture discriminability and short-term repeatability of the risk indices estimated from the automatic tool.

## Chapter 3

# Automation of DXA-based finite element modelling procedure for assessing hip fracture risk

### 3.1 DXA-based finite element modelling

DXA-based finite element model is a two-dimensional FE model constructed from DXA-scans. The methodology used to automate the DXA-based finite element modelling procedure and assess its feasibility in hip fracture risk assessment is shown in Figure 1. Fundamental steps involved were the automatic extraction of femur contour from DXA image, automatic detection of critical femur cross-sections and regions of interest (ROIs), finite element mesh generation, material properties assignment and the application of loading and boundary conditions. Then the model was solved for finite element solutions and results were post-processed to determine hip fracture risk indices. In the present study, to make the model patient-specific and automatic, all relevant information was

automatically extracted from the patient's clinical DXA scan. To assess the feasibility of clinical application, hip fracture discriminability of the risk indices was addressed. In material properties assignment stage, different material models were tested to select one that showed preliminary improvement in hip fracture discriminability. With that material model, hip fracture risk indices were calculated using two approaches i.e. femur cross-section and region of interest based. Besides, for comparison, HFRI were calculated at two types of region of interest such as self-defined and clinical ROI. Calculated hip fracture risk indices were transferred to medicine school for an independent and blind performance evaluation. The school provided an estimate for the hip fracture discriminability of indices in the form of the area under the receiver-operating-characteristics curve (AUC) value. The AUCs were compared with those for densitometric measurements to quantify the improvement in hip fracture discriminability. A significant increase in AUC will establish the superiority of the proposed tool over BMD measurements in hip fracture risk assessment.

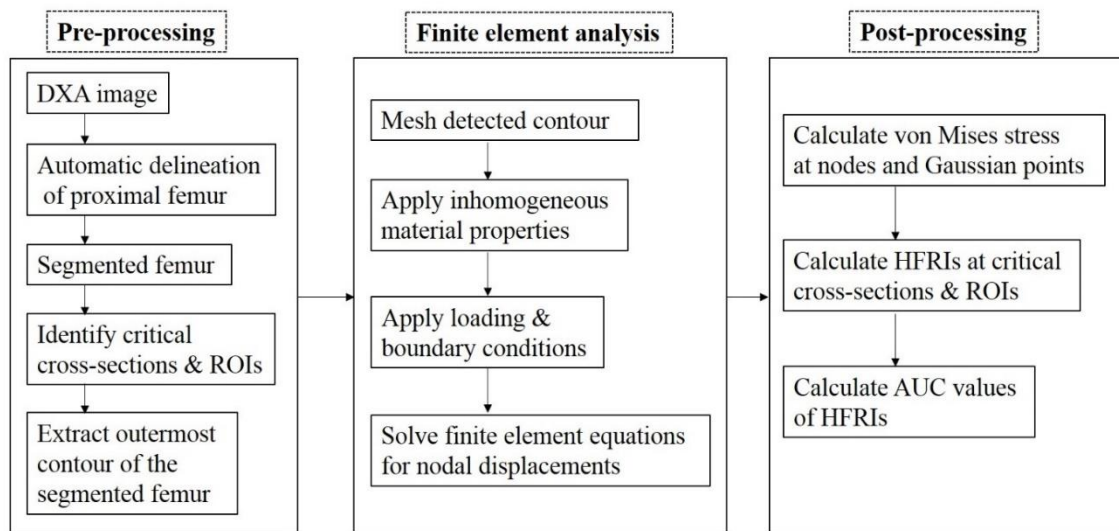


*Figure 1: The methodology to calculate hip fracture risk indices using automatic DXA-based FE method and assess hip fracture discriminability*

## 3.2 DXA-image

The BMD map extracted from the DXA scan is a two-dimensional gray-scale image representing pixel-by-pixel variation in BMD (Figure 2). In the present study, all subjects were scanned using a single fan-beam DXA scanner configuration ('GE Lunar Prodigy'). DXA images were accessed in both the native manufacturer format ('enCORE') and as a MATLAB file. The first file contains rectangular coordinates delimiting important regions of interest (ROIs) including femoral neck, head, shaft and trochanter in respective header files (see Figure 3). The second is a 16-bit integer image file representing BMD distribution in terms of pixel values. The ROIs enabled automatic segmentation of proximal femur and BMD information facilitated material property assignment in the FE model.

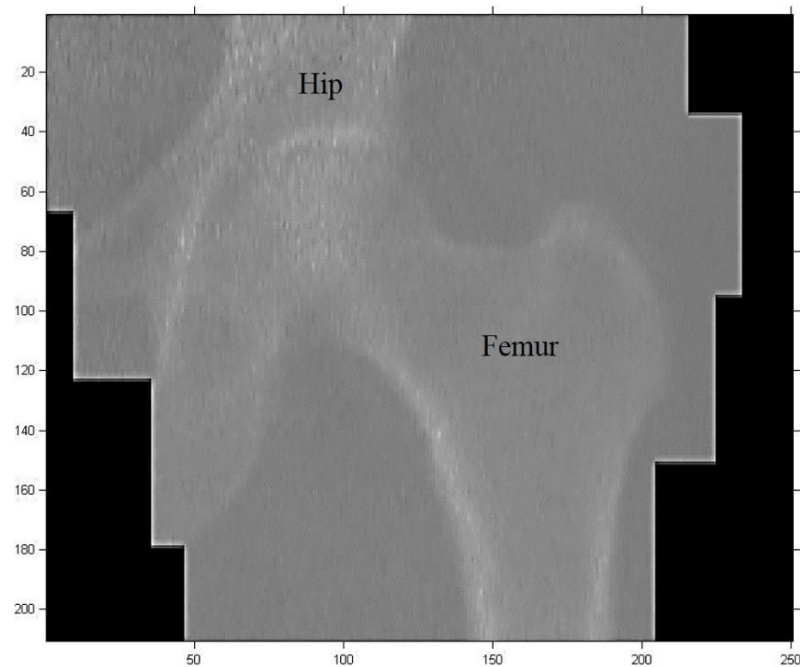


*Figure 2: A sample DXA image*



*Figure 3: Regions of Interest (ROIs) defined by the DXA scanner*

### 3.3 Automatic segmentation and generation of finite element mesh

The proximal femur was automatically segmented from the hip DXA scan and a finite element mesh was generated from the contour of the proximal femur. The step-by-step procedure to automatically segment the proximal femur is illustrated in Figure 4. Firstly, the hip and femoral shaft outline were detected from the DXA scan. Secondly, the portion of the hip outline above the femoral neck and head ROI was removed. Thirdly, a circle was fitted inside the head ROI. The two points on the circle closest to the medial and lateral shaft outline were identified, and the portion of the circle distal to those points was removed. Finally, any missing point between the head and shaft outline was interpolated

and outliers were removed. The boundary coordinates were saved and the finite element mesh was generated.

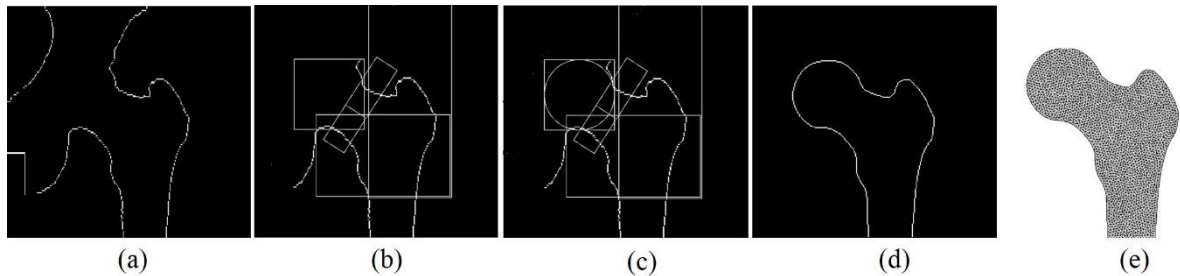


*Figure 4: Step-by-step procedure to segment proximal femur and mesh generation, (a) Hip-shaft outline (b) Shaft outline (c) Circle fitted inside head ROI (d) Segmented femur (e) Meshed femur*

### 3.4 Automatic detection of critical femur cross-sections and Regions of Interest (ROIs)

On the basis of clinical observations, hip fracture mostly happens at one of three critical locations, femoral neck, intertrochanter and femoral shaft [80-83]. Therefore, hip fracture risk has been calculated at the three critical cross-sections [33]. However, to maintain consistency with the clinical practice of BMD measurements and improve short-term reproducibility, hip fracture risk has also been defined in the regions of interest (ROIs) [37]. In the present study, hip fracture risk indices were calculated at different femur cross-sections and ROIs. For this purpose, critical femur cross-sections and ROIs were automatically detected in the DXA image.

### 3.4.1 Detection of critical femur cross-sections

Critical femur cross-sections, namely narrowest femoral neck, intertrochanter and subtrochanter are most prone to fracture. The section with the minimum diameter at the femoral neck is the narrowest femoral neck [84]. To locate the narrowest femoral neck, geometric information was extracted from ‘enCORE’ header file and MATLAB codes were developed to find the minimum width. The intertrochanteric cross-section is the line bisecting the femoral neck-shaft angle which is the angle formed by femoral neck axis and shaft axis [84]. Femoral neck axis is orthogonal to and bisects the narrowest femoral neck line. Femoral shaft axis is the central line of the femoral shaft [85] and its coordinates can be retrieved from ‘enCORE’ header file. Finally, the subtrochanteric cross-section was located at 1.5 times narrowest femoral neck width away from the femoral neck-shaft intersection point [84]. The identified femur cross-sections are shown in Figure 5.

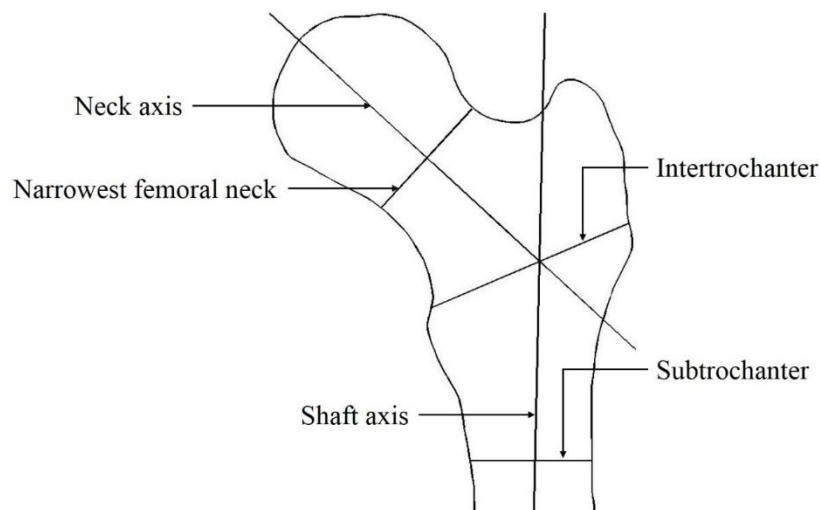


Figure 5: Critical cross-sections at proximal femur

### 3.4.2 Detection of Regions of Interest (ROIs)

In the present study, two types of regions of interest i.e. self-defined and clinical were used for comparative analysis. The self-defined regions of interest were 10mm wide rectangular regions placed around the three critical femur cross-section lines defined previously. Clinical regions of interest are inherent to DXA devices. MATLAB codes were used to extract coordinates corresponding to femoral neck, trochanteric and shaft regions of interest from 'enCORE' header files. Only the lower half of the DXA-scanner defined shaft ROI was used in the fracture risk index calculation to reduce its overlap with clinical trochanteric ROI. The total ROI includes the femur region between the proximal boundary of the femoral neck and the distal boundary of subtrochanteric/shaft ROI. Figure 6 shows the self-defined and clinical ROIs used for HFRI calculation.

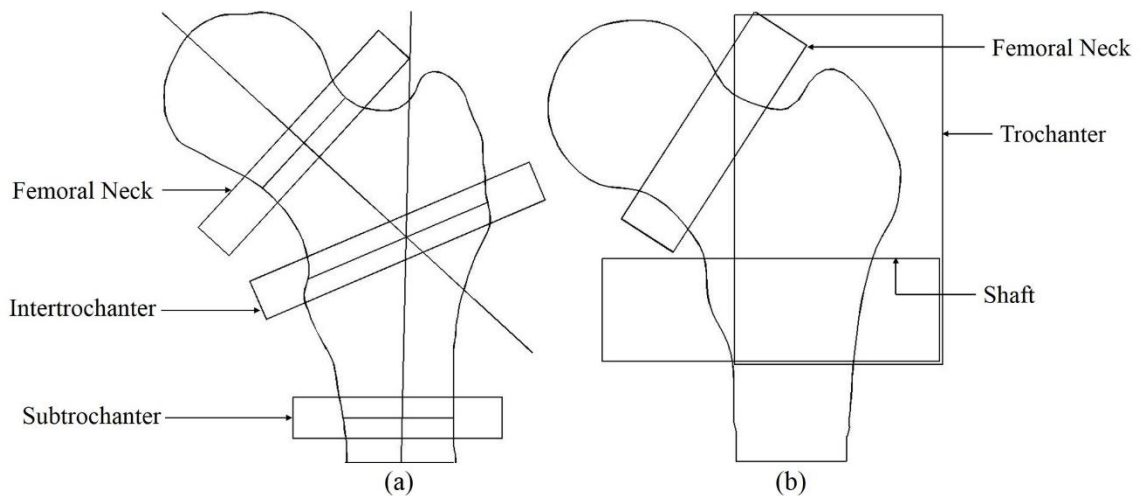


Figure 6: (a) Self-defined (10mm wide) and (b) Clinical regions of interest

## 3.5 Material models

Bone has inhomogeneous and anisotropic material properties. The DXA image captures inhomogeneity information by projecting BMD as pixel value in a two-dimensional coronal plane. Final stress/strain distribution depends on considering isotropic or anisotropic material properties [86]. However, anisotropy information is absent in the DXA images, therefore, we assumed an isotropic inhomogeneous material model. Considerably accurate results have been obtained by using isotropic material model in DXA-based FE models [17, 38]. Material properties were estimated from BMD. Initially, areal BMD ( $\text{g}/\text{cm}^2$ ) is derived from the DXA image [87]. Volumetric BMD ( $\text{g}/\text{cm}^3$ ) is estimated by dividing areal bone mineral density with subject-specific thickness derived in Section 3.6. Then, ash density  $\rho_{ash}$  (bone ash mass per unit volume) or apparent density  $\rho_{app}$  (hydrated tissue mass per unit volume) is estimated from volumetric BMD [87].

$$\rho_{ash} = \frac{vBMD}{1.14} \quad \left(\frac{\text{g}}{\text{cm}^3}\right) \quad (1)$$

$$\rho_{app} = \frac{\rho_{ash}}{0.598} \quad \left(\frac{\text{g}}{\text{cm}^3}\right) \quad (2)$$

Finally, bone material properties are estimated from either ash density or apparent density using empirical relations between them. Results from image-based finite element analysis largely depend on the adopted relationship between material properties and BMD. In the literature, many such relationships exist and which one perfectly describes bone material properties is a matter of dispute [88, 89]. In the present study, several material models were tested for the automatic tool. In general, finite element model was constructed using different material models and AUCs for HFRIs at clinical ROIs were obtained. Poisson's

ratio was considered constant with a magnitude of 0.3 [17] for all material models. As proximal femur behaves linearly elastic until failure [90], a linear elastic analysis excluding post-yield behavior was performed in this study.

Bone material properties refer to elastic and strength properties of bone. Usually, bone specimens are mechanically tested and regression analysis is performed to obtain empirical relationships between material properties and bone densities. Such relationship can be either linear or non-linear [91-95]. A systematic review of elasticity-density relationship can be found in Hegalson et al. [88]. Depending on the exponent of the density term reported there, in the present study, empirical relations were classified into three categories namely linear model, non-linear model with an exponent between 1-2 and 2-3. A representative was selected from each category for the comparison study. About bone strength, several researchers suggested a linear relationship between bone strength (yield or ultimate stress) and modulus [93, 89, 96, 94], while empirical relations have been developed to derive strength properties directly from BMD [92, 91, 93, 94]. Therefore, in the present study, separate finite element model was constructed for each of the three elasticity-density relationships and assuming a linear relationship between yield stress and Young's modulus. Later on, the strength-modulus relationship was replaced by strength-density relationship and finite element model was reconstructed for all three elasticity-density relationships.

While selecting elasticity-density relationship, preference was given to those defined over a large range of bone densities. If a single equation cannot be found, two equations, one for low density and the other for high density were used. If the density ranges did not

overlap, a third equation was developed by linear interpolation between the extremes of previous two equations [35].

Linear material model developed by Lotz et al. [92] and Li and Aspden [97] was used to derive Young's modulus ( $E$ ) from apparent density, for cortical and trabecular bone respectively. Although cortical and trabecular bone cannot be discriminated in a DXA-image, however, cortical bone was assumed to be a denser type of trabecular bone.

$$E(GPa) = \begin{cases} 0.573 * \rho_{app} - 0.0094, & \text{if } \rho_{app} < 1.20 \text{ g/cm}^3 \\ -13.43 + 14.261 * \rho_{app}, & \text{if } \rho_{app} \geq 1.20 \text{ g/cm}^3 \end{cases} \quad (3)$$

From the review paper [88] no non-linear elasticity-density relationship having exponent between 1 and 2 was found for higher BMDs ( $\rho_{app} > 0.90$ ). Meanwhile, Bujis et al. [36] constructed a validated two-dimensional finite element model where they estimated Young's modulus directly from areal BMD ( $\text{g/cm}^2$ ) using an optimized power regression model with an exponent between 1 and 2. The same relation was adopted here and thereby the assumptions associated with transforming areal BMD into volumetric BMD was avoided.

$$E(GPa) = 29.8 * \rho_{areal}^{1.56} \quad (4)$$

Non-linear relationships with density exponent between 2 and 3 proposed by Keyak et al. [93] and Keller [91] were used for deriving Young's modulus of trabecular and cortical bone respectively. One distinctive characteristic of these studies was a large number of samples used in the experiments. Original density range reported by the authors did not overlap and hence a third equation was developed for the missing range of BMD [35].

$$E(GPa) = \begin{cases} 33.9 * \rho_{ash}^{2.20}, & \text{if } \rho_{ash} \leq 0.270 \text{ g/cm}^3 \\ 10.5 * \rho_{ash}^{2.29}, & \text{if } \rho_{ash} \geq 0.60 \text{ g/cm}^3 \\ 5.307 * \rho_{ash} + 0.469, & \text{if } 0.27 < \rho_{ash} < 0.60 \text{ g/cm}^3 \end{cases} \quad (5)$$

Linear relationship between yield stress ( $Y$ ) and Young's modulus, as proposed by Morgan et al. [94], was adopted in the present analysis since their experimental protocol and specimen dimension was most accurate for determining bone mechanical properties [88]. Indeed, they observed a very high correlation between yield stress and Young's modulus ( $R^2 > 0.94$ ). While applying the relationships in the current study, yield stress was differentiated as tensile or compressive depending on principal stress state at Gaussian points. For very low value of  $E$ , the negative intercept of the linear equation was ignored.

$$Y(MPa) = \begin{cases} -0.41 + 0.0062 * E, & \text{Compressive} \\ 0.33 + 0.0039 * E, & \text{Tensile} \end{cases} \quad (6)$$

Afterward, yield stress was estimated from ash density [93, 91] and replaced Equation (6) in the finite element model.

$$Y(MPa) = \begin{cases} 137 * \rho_{ash}^{1.88} & \text{When } \rho_{ash} < 0.317 \text{ g/cm}^3 \\ 114 * \rho_{ash}^{1.72} & \text{When } \rho_{ash} \geq 0.317 \text{ g/cm}^3 \end{cases} \quad (7)$$

The best combination of Young's modulus and Yield stress approximation technique will produce highest AUC and that combination will be used to calculate HFRI and AUCs at femur cross-sections, over self-defined ROIs and repeatability analysis.

For a plane stress model, material property matrix  $D$  is expressed in terms of Young's modulus  $E$  and Poisson's ratio  $\nu$ .

$$D = \frac{E}{1-\nu^2} \begin{bmatrix} 1 & \nu & 0 \\ \nu & 1 & 0 \\ 0 & 0 & \frac{1-\nu}{2} \end{bmatrix} \quad (8)$$

To more precisely capture variation in BMD, material properties were assigned at element Gaussian integration points.

### 3.6 Plane stress model with triangular elements

A two-dimensional FE model can be constructed from DXA image. Assuming each femur as a plate, a plane stress model with subject specific thickness was selected for finite element simulations. Subject-specific thickness has previously been proposed for predicting femoral strength [38, 39]. It was assumed that the plate's cross-sectional area and moments of inertia at the narrowest femoral neck are equivalent to those of the femur. In the present study, patient-specific thickness  $t$  was defined as

$$t = \frac{3.5}{16} \pi * W \quad (9)$$

Where  $W$  is the width at the narrowest femoral neck.

For finite element simulation, three-node triangular elements were used. With respect to clinical applications, this represents a practical choice because of their computational efficiency and simplicity. Since finer mesh size improves performance at higher computational cost, a trade-off is made between mesh size and accuracy requirement. Usually, suitable mesh size is determined based on convergence test. A convergence study was performed at the clinical trochanteric region of interest as shown in Figure 7. On the basis of this convergence test, each finite element model consisted ~2500 nodes.

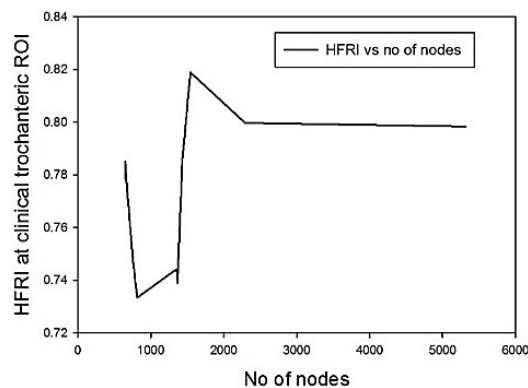


Figure 7: Convergence test at clinical trochanteric ROI

Relevant theory associated with two-dimensional finite element analysis with the triangular element is discussed here for completeness. In principle, a global stiffness matrix and a force vector are constructed from element level and solved for global degrees of freedom. The degrees of freedom are expressed as nodal displacements. Since three-node triangular elements are two dimensional, therefore, each node can have displacement components in x and y-direction only. Displacement of a particle inside a triangular element can be approximated by triangular element shape functions and element nodal displacements as [98]

$$\mathbf{u}^{(e)} = \mathbf{N}^{(e)T} \mathbf{U}^{(e)} \quad (10)$$

Where,  $\mathbf{N}^{(e)}$  is the matrix containing element shape functions and  $\mathbf{U}^{(e)}$  is the element nodal displacement vector. These can be expressed as [99]

$$\mathbf{N}^{(e)T} = \begin{bmatrix} N_1 & 0 & N_2 & 0 & N_3 & 0 \\ 0 & N_1 & 0 & N_2 & 0 & N_3 \end{bmatrix} \quad (11)$$

$$\mathbf{U}^{(e)T} = \{u_{x1}^{(e)} \quad u_{y1}^{(e)} \quad u_{x2}^{(e)} \quad u_{y2}^{(e)} \quad u_{x3}^{(e)} \quad u_{y3}^{(e)}\} \quad (12)$$

The shape functions and  $\mathbf{B}$  matrix for a linear triangular element can be expressed in terms of nodal coordinates and if physical coordinate system is used then,

$$\begin{Bmatrix} N_1 \\ N_2 \\ N_3 \end{Bmatrix} = \frac{1}{2\Delta^{(e)}} \begin{bmatrix} (x_2 y_3 - x_3 y_2) & y_{23} & x_{32} \\ (x_3 y_1 - x_1 y_3) & y_{31} & x_{13} \\ (x_1 y_2 - x_2 y_1) & y_{12} & x_{21} \end{bmatrix} \begin{Bmatrix} 1 \\ x \\ y \end{Bmatrix} \quad (13)$$

$$\mathbf{B}^{(e)T} = \frac{1}{2\Delta^{(e)}} \begin{bmatrix} y_{23}^{(e)} & 0 & y_{31}^{(e)} & 0 & y_{12}^{(e)} & 0 \\ 0 & x_{32}^{(e)} & 0 & x_{13}^{(e)} & 0 & x_{21}^{(e)} \\ x_{32}^{(e)} & y_{23}^{(e)} & x_{13}^{(e)} & y_{31}^{(e)} & x_{21}^{(e)} & y_{12}^{(e)} \end{bmatrix} \quad (14)$$

where,  $x_{mn} = x_m - x_n, y_{mn} = y_m - y_n$

Element stiffness matrix is constructed by integrating the product of  $\mathbf{B}$  and  $\mathbf{D}$  matrix as

$$\mathbf{k}^{(e)} = \int_{V^{(e)}} \mathbf{B}^{(e)T} \mathbf{D} \mathbf{B}^{(e)} dV \quad (15)$$

All entries in  $\mathbf{B}$  matrix and subject specific thickness are constant. Element volume is the product of element area and thickness. Material property matrix  $\mathbf{D}$  is a function of location and as mentioned in Section 3.6, it was defined at element gaussian integration points. Hence, element stiffness matrix was obtained by Gaussian integration.

Element stiffness matrix and element force vector is connected with each other through the element nodal displacement vector. The relationship is expressed as

$$\mathbf{k}^{(e)} \mathbf{U}^{(e)} = \mathbf{f}^{(e)} \quad (16)$$

Element connectivity table is used to assemble element stiffness matrix into global stiffness matrix ( $\mathbf{K}$ ), element degree of freedom ( $\mathbf{U}^{(e)}$ ) into global degree of freedom vector ( $\mathbf{U}$ ) and element force vector ( $\mathbf{f}^{(e)}$ ) into global force vector ( $\mathbf{F}$ ) and the global system of equations is formed. In matrix form, global system of equations can be written as

$$\mathbf{K} \mathbf{U} = \mathbf{F} \quad (17)$$

$$\text{where, } \mathbf{K} = \sum_{e=1}^n \mathbf{k}^{(e)}, \mathbf{U} = \sum_{e=1}^n \mathbf{U}^{(e)} \text{ and } \mathbf{F} = \sum_{e=1}^n \mathbf{f}^{(e)}$$

Where,  $n$  represents total the number of elements in the FE model. Following the global system of equation formation, boundary conditions are applied to prevent rigid body motion. Afterward, global system of equations is solved for global displacement of nodes from which element nodal displacements are extracted. After getting element nodal displacements, plane stress components of element strain  $\boldsymbol{\epsilon}^{(e)}$  and stress  $\boldsymbol{\sigma}^{(e)}$  can be calculated as:

$$\boldsymbol{\varepsilon}^{(e)} = \begin{Bmatrix} \varepsilon_x^{(e)} \\ \varepsilon_y^{(e)} \\ \gamma_{xy}^{(e)} \end{Bmatrix} = \mathbf{B}^{(e)} \mathbf{U}^{(e)} \quad (18)$$

$$\boldsymbol{\sigma}^{(e)} = \begin{Bmatrix} \sigma_x^{(e)} \\ \sigma_y^{(e)} \\ \tau_{xy}^{(e)} \end{Bmatrix} = \mathbf{D} \boldsymbol{\varepsilon}^{(e)} \quad (19)$$

### 3.7 Loading and boundary condition simulating a sideways fall

Based on previous studies, falls are responsible for more than 90% of hip fractures among elderly people [3, 100], and sideways falls are most often responsible for hip fractures [65, 66]. Consequently, hip fracture risk for a sideways fall from standing height was analyzed. Figure 8 shows a typical sideways fall on greater trochanter [103]. To assess hip fracture risk, individual peak impact force ( $F$ ) was estimated from subject-specific anthropometric parameters such as body height ( $h$ ) and weight ( $w$ ) [101-103].

$$F = 8.25 * w \left( \frac{h}{170} \right)^{\frac{1}{2}} N \quad (20)$$

Where,  $h$  is in centimeter (cm) and  $w$  in Newton (N). The force was applied in pressure form on the greater trochanter [98]. For this purpose, element edges located on the boundary of greater trochanter were identified and pressure load was converted into equivalent nodal forces of contributing elements. All these steps were performed automatically.

A boundary condition simulating sideways fall was adopted for all cases. Medial displacement of the femoral head was prevented [38, 39] and the distal end of the proximal femur was considered fixed [33, 37-39]. Figure 9 shows the loading and boundary condition used in the current analysis.

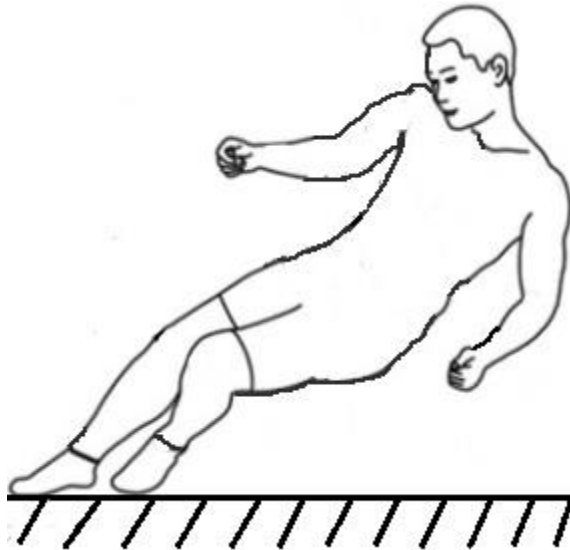


*Figure 8: A typical sideways fall*

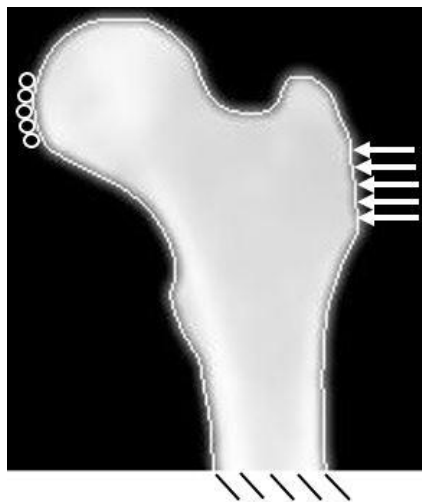


*Figure 9: Loading and boundary condition simulating a sideways fall*

# Chapter 4

## Calculation of hip fracture risk indices

### 4.1 Hip fracture risk indices

From the literature, it can be observed that two types of biomechanical risk indices i.e. load-to-strength ratio (LSR) or factor of risk [38, 104-107] and fracture risk index (FRI) [33, 37, 108, 109] have been proposed to assess the osteoporotic fracture risk. While LSR is a global criterion, FRI is a local measurement of fracture risk. LSR considers applied load and strength of the whole femur to determine fracture risk and its applicability is limited to specifying types of hip fracture i.e. intracapsular or extracapsular. FRI is a function of location, therefore able to assess the risk of fracture at a particular location of femur such as at femoral neck or trochanter. The technique of local fracture risk assessment has been adopted in the current study.

In the literature, local fracture risk indices were calculated either by a cross-section or region of interest based approach [33, 37]. Although Luo et al. [37] argued the superiority of later approach, however, hip fracture discriminability of two approaches was not

compared. Therefore, in the current analysis, fracture risk indices were calculated using both approaches (Figure 5 & Figure 6) and area under the receiver-operating-characteristics curve (AUC) was used to contrast their performances. Local fracture risk indices were calculated at two types of ROIs, i.e. self-defined and clinical (Figure 6) to analyze the effect of ROI definition on AUC. The latter ROI is larger in size and well defined compared to the former one.

The definition of hip fracture risk indices originally developed by Luo et al. [33, 37] was used in the current study. Those were defined based on allowable stress method excluding the post-yield behavior of proximal femur [20]. In general, fracture risk indices were expressed as a ratio of effective or von Mises stress induced by the external force and the yield stress of the cross-section or ROI under consideration.

#### 4.1.1 HFRI at critical femur cross-section

Hip fracture risk indices were calculated at critical femur cross-sections detected before (Figure 5). It was assumed that a cross-section will fracture if effective stress exceeds maximum sustainable stress (yield stress) at that cross-section. Thus, cross-section HFRI was defined as the average ratio of effective and yield stress of all points lying along the cross-section line:

$$\eta = \text{average} \left( \frac{u}{u_Y} \right) \quad (21)$$

Where  $u$  and  $u_Y$  symbolize effective and yield stress of the points along the femur cross-section respectively.

The effective stresses at points on three critical femur cross-sections were calculated by post processing the nodal displacements attained from the solution of system of Equations

(17). Firstly, constant element strains were found from strain-displacement matrix presented in Equation (18). Then nodal strain was calculated as the average strain of the elements sharing the common node. The plane stress components of nodal stress were obtained from material's constitutive relationship in Equation (19), where Young's modulus ( $E$ ) was defined at element nodes. Finally, nodal von Mises stress was calculated as [110, 111]:

$$\sigma_{n,VM} = \frac{1}{\sqrt{2}} * \sqrt{(\sigma_x - \sigma_y)^2 + \sigma_x^2 + \sigma_y^2 + 6 * \tau_{xy}^2} \quad (22)$$

Where,  $\sigma_{n,VM}$  is the effective nodal stress and  $\sigma_x$ ,  $\sigma_y$ ,  $\tau_{xy}$  are plane stress components.

Nodal yield stress was estimated from nodal ash density using Equation (7). Once nodal effective and yield stress were computed, then they were mapped along a cross-section line using nearest neighbor interpolation. Afterward, their ratio was obtained and averaged to get HFRI at the cross-section under consideration.

#### 4.1.2 HFRI at Region of interest (ROI)

Over an ROI, HFRI is defined as a mean ratio between effective stress caused by external force and yield stress of the femur bone over the ROI. Symbolically, hip fracture risk index at an ROI [37] is given as:

$$\eta_{ROI} = \frac{\sum_{i=1}^N \int_{A_i} \frac{\sigma_{eff}}{\sigma_Y} dA}{\sum_{i=1}^N A_i} \quad (23)$$

Where,  $A_i$  ( $i=1, 2, \dots, N$ ) are  $N$  finite element areas within the ROI.  $\sigma_{eff}$  and  $\sigma_Y$  are effective or von Mises and yield stress, respectively. To capture variation in BMD more precisely, those parameters were calculated at element Gaussian integration points.

Effective stresses at element Gaussian integration points were approximated from finite element solutions. Initially, element strain was calculated from nodal displacements using strain-displacement relationship in Equation (18). Three node triangular elements are constant strain triangles. Hence, plane stress components at a Gaussian point inside the triangular element was calculated from material's constitutive relationship in Equation (19). In material matrix ( $\mathbf{D}$ ), the Young's modulus ( $\mathbf{E}$ ) was the Young's modulus at Gaussian point. Then effective stress was calculated from plane stress components using Equation (22). Yield stress at element Gaussian integration point was estimated from either apparent density or ash density at that point, using Equation (6) or (7). While implementing Equation (6), principal stress (tensile or compressive) at Gaussian point was estimated from plane stress components at that point as:

$$\sigma_{1n}, \sigma_{2n} = \frac{\sigma_x + \sigma_y}{2} \pm \sqrt{\left(\frac{\sigma_x - \sigma_y}{2}\right)^2 + \tau_{xy}^2} \quad (24)$$

While using Equation (7), compressive yield stress was directly computed from ash density and no distinction was made between tensile and compressive yield stress.

After calculating effective and yield stress at Gaussian points, their ratio was obtained.

Subsequently, seven points Gaussian quadrature rule was applied to all elements inside the

ROI under consideration and averaged to get HFRI at that ROI.

# Chapter 5

## Clinical studies

### 5.1 Short-term repeatability

In the medical field, assessment of a diagnostic technique's reproducibility is of high importance because it directly influences the diagnostic power of the technique. A diagnostic technique needs to be highly reproducible to detect small changes in the parameter under consideration such as bone quality. Bone mineral density measurements have been proved to be highly reproducible and hence adopted in the clinics for osteoporosis screening. For the hip fracture risk indices estimated from the automatic FE tool, they must have acceptably high reproducibility before the tool could be implemented in clinics for fracture risk assessment.

Short-term repeatability is a statistical measure of precision and calculated from longitudinal data collected from patients. If two scans are taken from the same patients within a sufficiently short interval of time (less than 28 days), HFRI calculated from paired cans should be the same assuming that negligible change in BMD. Since bone mineral

density changes at a slow rate [112], hence the assumption made can be considered valid. The coefficient of variation (CV) provides a measure of repeatability that is widely used in bone densitometry [112]. This parameter was adopted in the present study to measure the precision error in calculated HFRI. Paired scans were taken from 108 patients as part of a routine quality assurance program and HFRI were calculated. Contours segmented from the two repeat scans had equal lengths and all other factors related to finite element analysis were kept same for consistency. The CV of HFRI at each ROI was computed separately using following equations [112]:

$$CV = \sqrt{\frac{\sum_{j=1}^m CV_j^2}{m}} \quad (25)$$

$$CV_j = \frac{SD_j}{\bar{x}_j} \quad (26)$$

$$\bar{x}_j = \frac{x_j^{(1)} + x_j^{(2)}}{2} \quad (27)$$

$$SD_j = \sqrt{\frac{1}{2} \left[ \left( x_j^{(1)} - \bar{x}_j \right)^2 + \left( x_j^{(2)} - \bar{x}_j \right)^2 \right]} \quad (28)$$

Where,  $x_j^{(1)}$  and  $x_j^{(2)}$  are first and second measurement of HFRI respectively and  $\bar{x}_j$  is the mean of them.  $SD_j$  is the standard deviation of case  $j$ , and  $m$  is the total number of cases acquired. Since each pixel in a DXA-image is a measure of total bone mass along a vertical ray traversing the bone at the pixel location [28], therefore in-house areal BMD was calculated as average BMD of all DXA-image pixels inside an ROI and CV was calculated accordingly. After initial calculation of CVs, cases with highest differences in repeat femoral neck HFRI were identified and after visual inspection for poor contours or

inconsistent ROI positions, thirty such cases were incrementally removed from analysis to analyze their effect on repeatability.

## 5.2 Discrimination ability in a small-scale retrospective clinical study

It is imperative to clinically evaluate the accuracy of a diagnostic test before it can be deployed for actual screening. Usually either a prospective or retrospective study is conducted on a representative population. The fundamental objective is to analyze how well diseased and normal group of patients can be separated by the test results. In the medical area, receiver operating characteristic (ROC) curve is extensively used to assess classification accuracy of a diagnostic test.

A prospective or retrospective longitudinal study enables to obtain a true classification of the diseased and normal group. While prospective study moves forward with time, the retrospective study looks backward and examines past data to analyze exposure to a disease. A prospective study is time-consuming, expensive and difficult to monitor. If a proper database is maintained, the retrospective study is more convenient to conduct. In the present study, a retrospective clinical study was performed on the cases selected from a well-maintained database. Hip fracture risk indices were calculated by automatic DXA-based FE tool and ROC analysis was performed to test discriminability of the HFRIIs. A detailed procedure to develop ROC curve can be found in Fawcett [113]. Here a short summary is presented for convenience.

In an ROC curve, true positive rate (TPR) or sensitivity is plotted against false positive rate (FPR) or 1-specificity (see Figure 10). There could be four outcomes by a diagnostic test, a correct identification of diseased and normal case, a normal case can be identified as diseased or vice versa. TPR is the likelihood to identify diseased cases correctly and FPR is the probability of misidentifying normal cases. A threshold or cut-off value for the diagnostic result (in our case HFRI) is determined and TPR, FPR is calculated and plotted. The threshold is varied within the entire range of diagnostic result (HFRI) and the whole ROC curve is obtained. Afterward, the area under the ROC curve (AUC) is calculated which represents the discrimination ability of the diagnosis technique. An AUC equals to unity denotes perfect classification while an area of 0.5 suggests the inability of discrimination. The 95% confidence interval is also calculated which denotes the interval within which true AUC lies with 95% confidence. In the current analysis, calculated HFRI were transferred to the medicine school for an independent and blind evaluation of the accuracy of the HFRI.

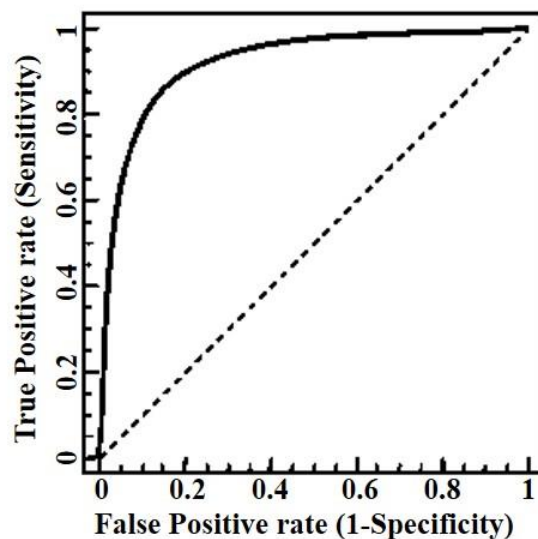


Figure 10: A sample ROC curve

## 5.3 Clinical cases extracted from Manitoba Bone Mineral Density Database for the studies

All clinical cases were extracted from Manitoba Bone Mineral Density Database in an anonymous way under a human research ethics approval. A total of 390 cases were analyzed with the automatic DXA-based finite element tool. All subjects were elderly women with an age between 64 to 99 years (average 75 years). Body Mass Index (BMI) was calculated for each case and all other relevant information such as body height, body weight, regions of interest, etc., were embedded in the DXA files as previously described. Statistical information of all cases is listed in Table 1.

*Table 1: Demographic information for the 390 clinical cases*

| Attributes         | Age (years) | Height (cm)   | Body weight (kg) | BMI (kg/m <sup>2</sup> ) |
|--------------------|-------------|---------------|------------------|--------------------------|
| Range              | 64-99       | 138.43-175.26 | 32.20-105.23     | 15.58-39.92              |
| Average            | 75          | 158.30        | 63.83            | 25.40                    |
| Standard deviation | 6.90        | 6.25          | 11.41            | 4.03                     |

# Chapter 6

## Results

Calculation of HFRIIs using automatic DXA-based finite element tool was succeeded by the area under the ROC curve (AUC) calculation. The significance of automatic FE tool derived HFRIIs was measured with respect to baseline AUC for BMD. At first, different material models were tested at clinical ROIs and then with the best material model, HFRIIs were calculated at critical femur cross-sections and over self-defined ROIs. For comparison, AUCs for femoral neck BMD and total hip BMD were also calculated. All computed AUC values were statistically significant ( $P < 0.001$ ).

All results are reported in this chapter. In Section 6.1, AUC values for HFRIIs calculated at clinical ROIs using different material models are presented. AUCs for HFRIIs calculated at the three critical femur cross-sections (Figure 5), self-defined (10mm wide) and clinical ROIs (Figure 6) with an identical material model are reported in Section 6.2. Section 6.3 contains correlation results between densitometric measurements and HFRIIs. Short-term precision study results are presented in Section 6.4.

## 6.1 AUCs for different material models

Three types of Young's modulus-density relationship and two types of yield stress approximation technique have been tested here. When a linear relation between yield stress and Young's modulus was assumed (Figure 11 and Table 2), linear material model had significantly higher AUCs than femoral neck BMD (AUC 0.713) at trochanteric (AUC 0.735) and total ROI (AUC 0.724), alike the non-linear model with an exponent between 1 and 2 (AUC 0.761 and 0.746 respectively for trochanteric and total ROI) . None but the non-linear material model with an exponent between 1 and 2 produced AUC higher than the total hip BMD AUC (AUC 0.750) at the trochanteric ROI. Non-linear material model with an exponent between 2 and 3 had lowest AUCs at all ROIs compared to any other material models. For all material models, AUCs at femoral neck and shaft ROIs were always below femoral neck BMD AUC.

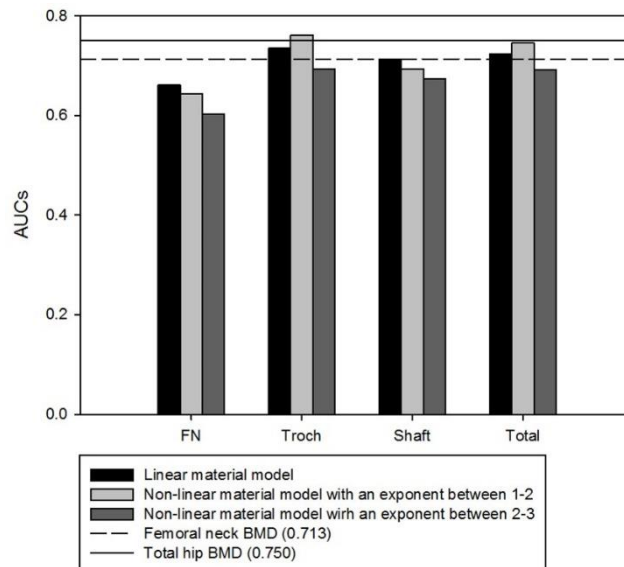


Figure 11: AUCs at clinical ROIs when yield stress was derived from Young's modulus

Table 2: AUCs (95% CI) for HFRI when yield stress was derived from Young's modulus

| Type of relationship<br>between Young's<br>modulus & BMD | Clinical ROIs          |                        |                        |                        |
|--|------------------------|------------------------|------------------------|------------------------|
|  | Femoral<br>Neck        | Trochanter             | Shaft                  | Total                  |
| Linear   | 0.661<br>(0.592,0.730) | 0.735<br>(0.676,0.794) | 0.713<br>(0.648,0.778) | 0.724<br>(0.664,0.784) |
| Nonlinear with<br>exponent between 1-2                   | 0.644<br>(0.572,0.715) | 0.761<br>(0.703,0.819) | 0.693<br>(0.627,0.760) | 0.746<br>(0.686,0.807) |
| Nonlinear with<br>exponent between 2-3                   | 0.603<br>(0.531,0.674) | 0.693<br>(0.627,0.758) | 0.674<br>(0.605,0.743) | 0.691<br>(0.624,0.757) |

When the yield stress approximation technique was changed, it increased AUCs from previous technique (Figure 11 and Table 2) for non-linear material models, irrespective of ROIs (Figure 12 and Table 3). In fact, a significant increase from total hip BMD AUC was achieved at the trochanteric ROI for both non-linear material models (AUC 0.771 and 0.775 respectively for material model with an exponent between 1-2 and 2-3). At total ROI, non-linear material models also produced AUCs higher than total hip BMD AUC (AUC 0.766 and 0.771 respectively for material model with an exponent between 1-2 and 2-3). Interestingly, between the two non-linear material models, the non-linear material model with an exponent between 2 and 3 produced slightly higher AUCs at all ROIs than the other non-linear material model. AUCs for linear model decreased from what it was previously (Figure 11), except at shaft ROI. For all material models, AUCs for shaft ROI were higher than femoral neck BMD AUC. Again, AUCs at femoral neck ROI were lower than femoral neck BMD for all material models.

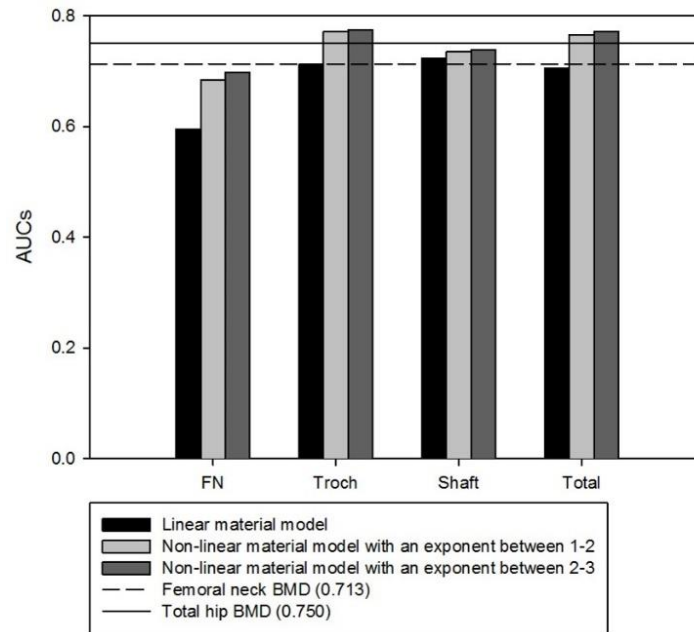


Figure 12: AUCs at clinical ROIs when Yield stress was derived from BMD

Table 3: AUCs (95% CI) for HFRIIs when yield stress was derived from BMD

| Type of relationship between Young's modulus & BMD | Clinical ROIs          |                        |                        |                        |
|--|------------------------|------------------------|------------------------|------------------------|
|  | Femoral Neck           | Trochanter             | Shaft                  | Total                  |
| Linear   | 0.595<br>(0.525,0.665) | 0.712<br>(0.650,0.775) | 0.723<br>(0.659,0.787) | 0.706<br>(0.643,0.769) |
| Nonlinear with exponent between 1-2                | 0.684<br>(0.615,0.752) | 0.771<br>(0.715,0.827) | 0.736<br>(0.672,0.800) | 0.766<br>(0.709,0.824) |
| Nonlinear with exponent between 2-3                | 0.698<br>(0.630,0.766) | 0.775<br>(0.719,0.831) | 0.739<br>(0.675,0.802) | 0.771<br>(0.714,0.827) |

## 6.2 AUCs at critical femur cross-sections, self-defined & clinical Regions of Interest (ROIs) for identical material model

Non-linear material model with an exponent between 2 and 3 and the technique of directly estimating yield stress from BMD was used to calculate HFRI at critical femur cross-sections and self-defined ROIs. From Figure 13 and Table 4 it can be seen that femur cross-section based and self-defined ROI based HFRI have comparable AUCs. Among three femur cross-sections (see Figure 5), the intertrochanteric cross-section had maximum discriminability (AUC 0.742). Alike intertrochanteric cross-section, intertrochanteric ROI had maximum AUC (AUC 0.744) among the three 10mm wide ROIs (see Figure 6a). A significant increase from femoral neck BMD (AUC 0.713) was achieved at the intertrochanteric cross-section and self-defined intertrochanteric ROI. Only the AUC at self-defined total ROI (AUC 0.778) was significantly higher than total hip BMD (AUC 0.750) and comparable to AUC at clinical total ROI (AUC 0.771). Turning to the AUCs at other locations (femoral neck and subtrochanteric cross-sections and self-defined ROIs), none was higher than femoral neck BMD AUC. AUC at clinical femoral neck ROI (AUC 0.698) was comparable to that of femoral neck cross-section and self-defined ROI (AUC 0.699 and 0.691 respectively). AUCs at clinical trochanteric ROI (AUC 0.775) was significantly higher than total hip BMD AUC and corresponding trochanteric cross-section and self-defined trochanteric ROI. AUC at clinical shaft ROI (AUC 0.739) was also higher

than the subtrochanteric cross-section (AUC 0.672) and 10mm wide subtrochanteric ROI (AUC 0.670).

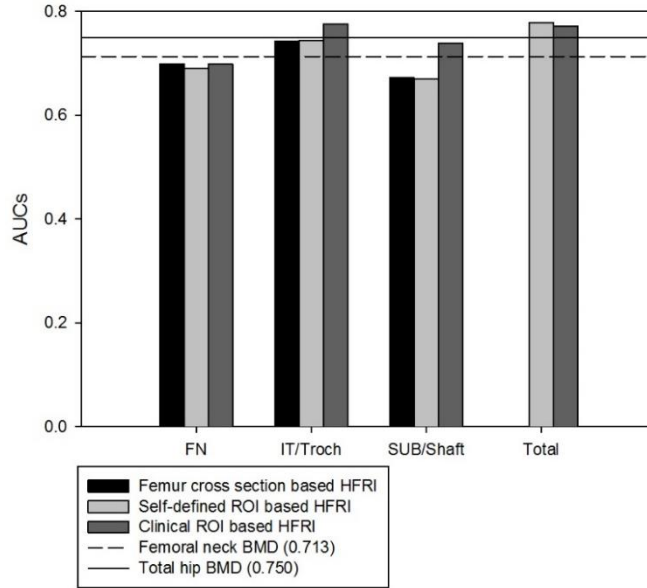


Figure 13: AUCs for HFRI calculated at femur cross-sections, self-defined and clinical ROIs when identical material model was used in FE analysis

Table 4: AUCs (95% CI) for HFRI calculated with different approaches but identical material model

| Critical cross-sections | AUCs (95% CI)          | Self-defined ROIs | AUCs (95% CI)          | Clinical ROIs | AUCs (95% CI)          |
|-------------------------|------------------------|-------------------|------------------------|---------------|------------------------|
| FN                      | 0.699<br>(0.632,0.765) | FN                | 0.691<br>(0.623,0.758) | FN            | 0.698<br>(0.630,0.766) |
| INT                     | 0.742<br>(0.683,0.800) | INT               | 0.744<br>(0.685,0.802) | Troch         | 0.775<br>(0.719,0.831) |
| SUB                     | 0.672<br>(0.605,0.739) | SUB               | 0.670<br>(0.603,0.737) | Shaft         | 0.739<br>(0.675,0.802) |
| -                       | -                      | Total             | 0.778<br>(0.722,0.834) | Total         | 0.771<br>(0.714,0.827) |

## 6.3 Correlation analysis

The correlation analysis was performed at clinical ROIs. To observe the pattern of mean HFRI, average values for HFRI at clinical ROIs were also calculated. Figure 14 presents the correlations among the four sets of HFRI and areal BMDs. Significant ( $P < 0.001$ ) negative correlation was observed between HFRI and areal BMDs. Correlation between femoral neck HFRI and areal BMD was lowest (0.772) while HFRI at other three ROIs correlated very well ( $> 0.80$ ) with respective areal BMDs. Femoral neck in-house areal BMDs and true (clinical) areal BMDs had strong ( $P < 0.001$ ) positive correlation (Figure 15). When average values of HFRI were calculated, the highest value appeared at the femoral neck followed by trochanteric, total and shaft region (Figure 16).

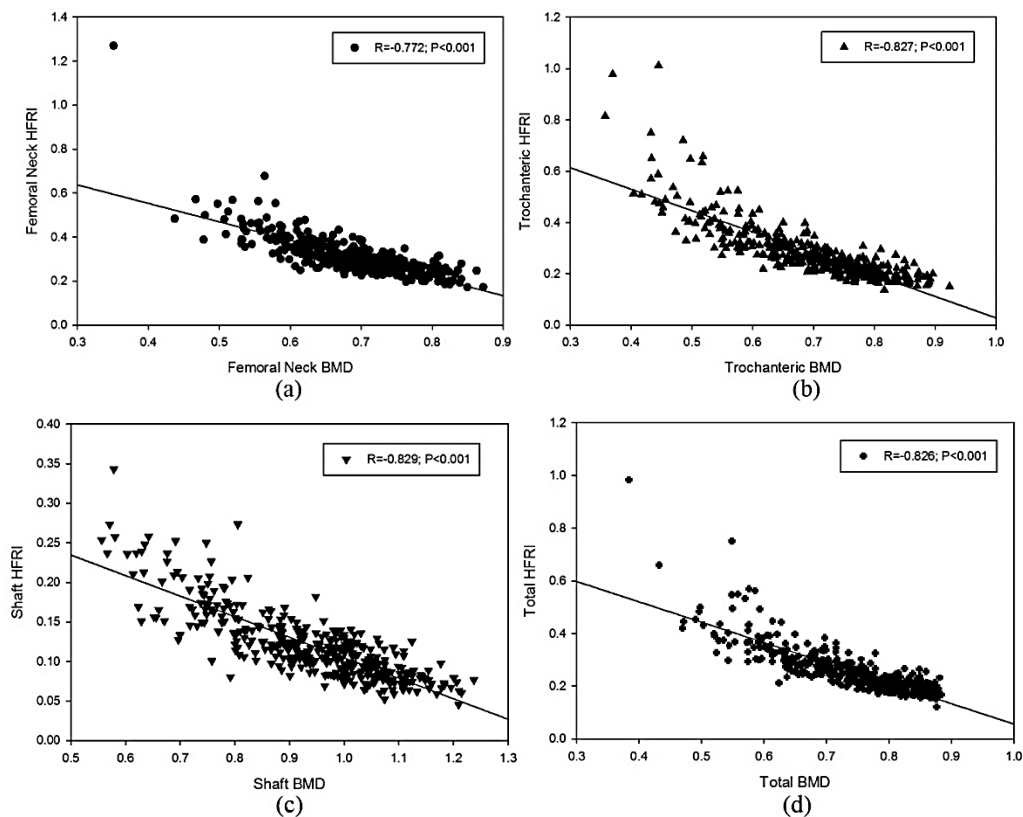


Figure 14: Correlation between HFRI and in-house BMD at clinical (a) Femoral neck (b) Trochanter (c) Shaft and (d) Total ROI

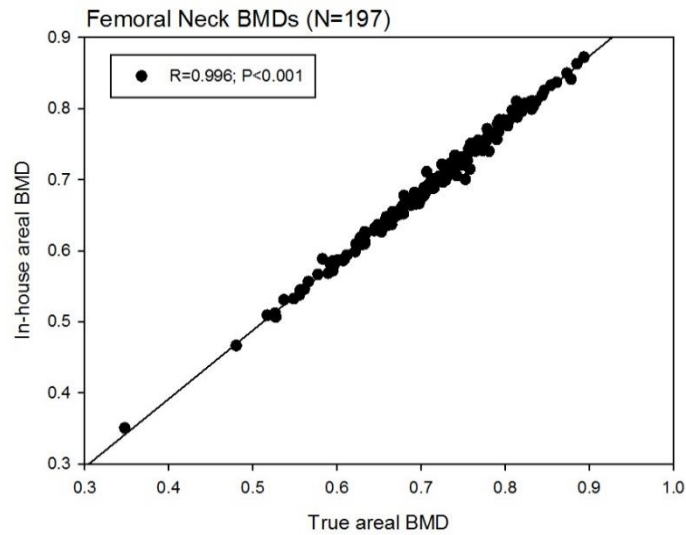


Figure 15: Correlation between in-house and true areal BMD at clinical femoral neck ROI

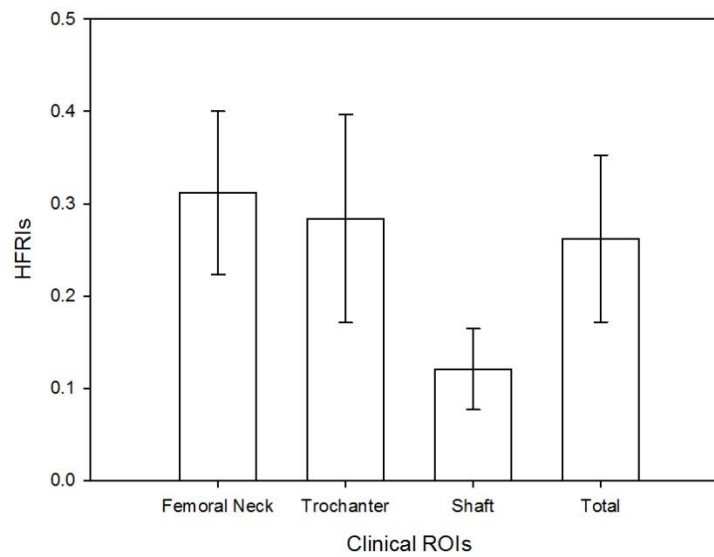


Figure 16: Mean and standard deviation of HFRI at clinical ROIs

## 6.4 Short-term repeatability of HFRI

Short-term repeatability of HFRI and in-house areal BMDs calculated at clinical ROIs are presented in Table 5 and Table 6. For 108 cases, it was found that HFRI and areal BMD at clinical total ROI had the highest reproducibility followed by trochanteric and femoral neck

ROI. Poor repeatability of HFRI was observed at the shaft ROI. Areal BMDs had good repeatability at all ROIs (Table 6).

After visual inspection, thirty cases were removed incrementally; ten cases at a time. Figure 17 shows ten representative worst cases removed from repeatability analysis. After successive removal of 30 poor scan pairs, repeatability of HFRI improved substantially (Table 5). CVs for HFRI were less than 3% at all ROIs excluding shaft ROI. Change in CVs for areal BMDs was not as dramatic as for HFRI, for example, repeatability of femoral neck areal BMD improved about 14% while improvement in femoral neck HFRI was approximately 45%. The highest amount of improvement in CV was associated with femoral neck HFRI followed by trochanteric (21%) and total HFRI (20%). Least amount of change in CV was observed for femoral shaft HFRI (approximately 3%).

*Table 5: CVs (%) for HFRI at clinical ROIs*

| No. of cases<br>(N) | Clinical ROIs |            |       |       |
|---------------------|---------------|------------|-------|-------|
|                     | Femoral neck  | Trochanter | Shaft | Total |
| 108                 | 3.53          | 3.29       | 4.18  | 2.92  |
| 98                  | 2.63          | 3.07       | 4.08  | 2.69  |
| 88                  | 2.33          | 2.69       | 3.97  | 2.44  |
| 78                  | 1.94          | 2.58       | 4.05  | 2.33  |

*Table 6: CVs (%) for areal BMDs at clinical ROIs*

| No of cases<br>(N) | Clinical ROIs |            |       |       |
|--------------------|---------------|------------|-------|-------|
|                    | Femoral neck  | Trochanter | Shaft | Total |
| 108                | 1.3           | 1.29       | 0.88  | 0.75  |
| 98                 | 1.21          | 1.32       | 0.86  | 0.75  |
| 88                 | 1.21          | 1.14       | 0.83  | 0.70  |
| 78                 | 1.12          | 1.16       | 0.82  | 0.70  |

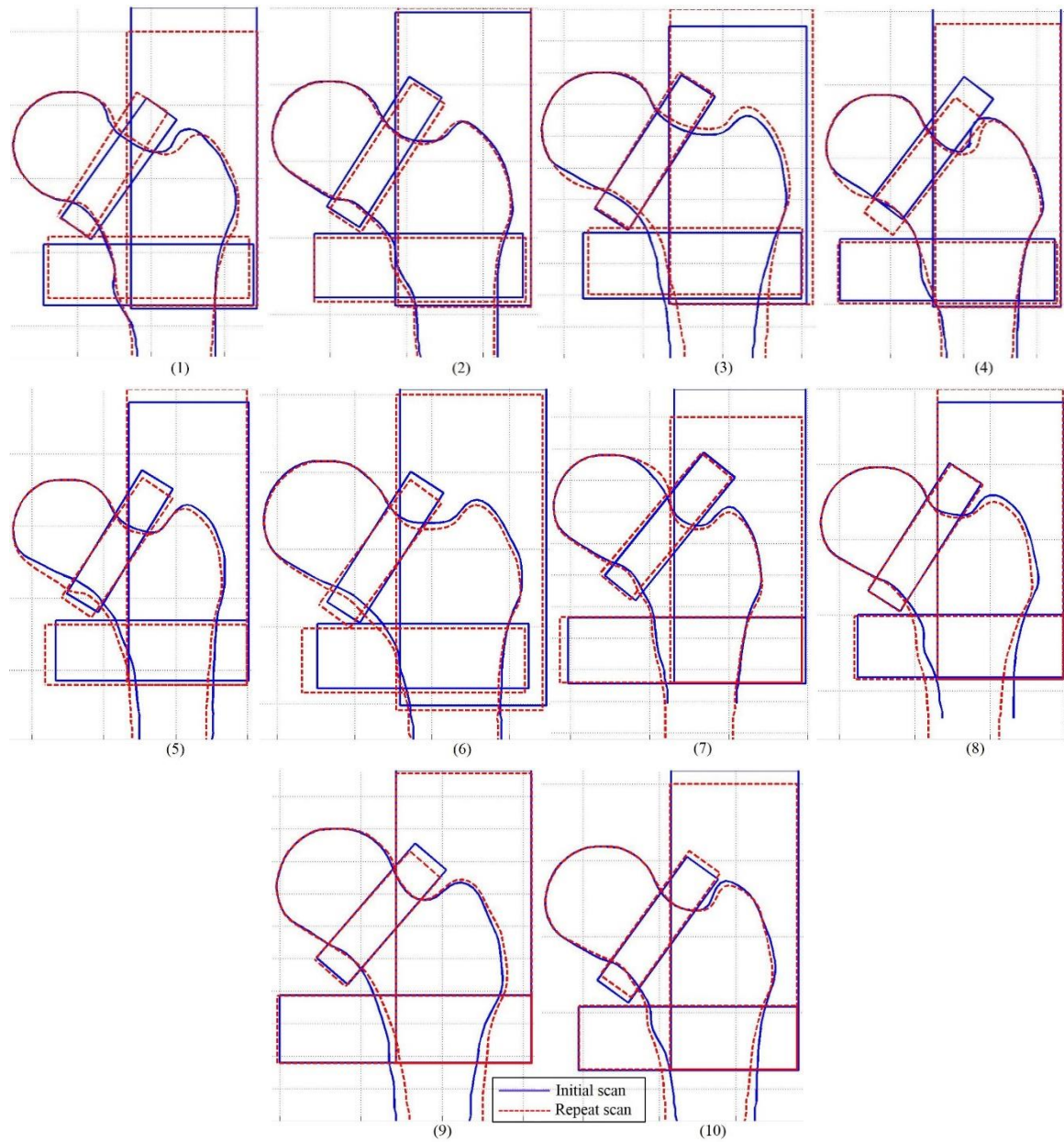


Figure 17: Ten representative cases responsible for poor repeatability in HFRIs

# Chapter 7

## Discussion

### 7.1 Assessment of hip fracture discriminability of HFRIIs

The hip fracture discriminability of the HFRIIs was estimated by calculating the area under the ROC curve (AUC). The closer the area to unity, the better is the discriminability. In the following sub-sections, discriminability of different material models, relative discriminability of two approaches (femur cross-section and ROI based) and two types of ROIs (self-defined and clinical) will be discussed. The improvement in AUC will be judged against AUCs found for femoral neck and total hip BMD.

#### 7.1.1 AUCs for different material models

From Figure 11 and Figure 12, it is evident that AUC changes when the material model is changed in the finite element analysis. Each material model was developed from different densitometric measurements and strain rates. Hegalson et al. [88] normalized various

elasticity-density relationships in terms of those two parameters and yet found substantial inter-study differences. Testing set-up, specimen size and geometry, site for specimen collection, type of bone considered, sample size, all determine the performance of a regression equation developed from a particular experiment [88].

Li and Aspden [97] collected cancellous bone cylindrical specimens from seven normal femoral heads samples and conducted unconstrained compression test (platen test). On the other hand, Lotz et al. [92] gathered 49 rectangular flat specimens of cortical bone from the metaphyseal shell of the proximal femur (femoral neck) and performed three-point bending test. Both studies yielded a linear relationship between elastic modulus and bone density. Morgan et al. [94] collected cylindrical trabecular specimens from different anatomical sites of the proximal femur (femoral neck & greater trochanter) of 61 donors and conducted uniaxial compressive and tensile mechanical testing (end cap and platen technique). They pooled data into a linear regression equation to derive compressive and tensile yield stress from Young's modulus. Keller et al. [91] collected 297 cubic femoral bone specimens from the region between lesser trochanter and lateral supra-condylar ridge (femoral shaft) and did a uniaxial compression test to correlate modulus and strength properties to bone density. Keyak et al. [93] harvested 36 cubical trabecular bone specimens of the proximal tibia from human cadavers and performed mechanical testing in different directions (superior-inferior, mediolateral and anteroposterior). Empirical relation between elasticity-density and yield stress-density was proposed for each direction, however, only equations developed for superior-inferior direction has been used in the present study since DXA-image is projected on a coronal plane. Bujis et al. [36] used

digital image correlation and mechanical testing to establish an empirical relation between Young's modulus and areal BMD.

When the linear elasticity-density relationship was combined with the linear yield stress-modulus relationship (Figure 11), an increase in AUC from femoral neck BMD may be attributed to the similarity in harvesting site (femoral neck) and specimen shape (cylindrical) used by Lotz et al. [92] and Morgan et al. [94] respectively in mechanical testing. Additionally, Morgan et al. [94] took samples from greater trochanter, which could also be the reason for good AUC at trochanteric, shaft and total ROI. On the other hand, failure to improve AUC beyond total hip BMD AUC could be the result of discrepancy in specimen shapes and collection sites. This hypothesis is further supported by the reduction in AUCs when yield stress-density equation was developed using cubic specimens collected from proximal tibia and shaft and combined with linear elasticity-density relationship developed from flat and cylindrical specimen harvested from femoral neck and head (Figure 12). Possibly the same fact is responsible for poor AUCs when a non-linear material model with an exponent between 2 and 3 (cubic specimen collected from proximal tibia and shaft) was combined with linear yield stress-modulus relationship (cylindrical specimen collected from femoral neck and greater trochanter) as seen in Figure 11. Indeed, combining yield stress-density relationships [91, 93] with elasticity-density [91, 93] equations developed from cubic specimens collected from similar sites (proximal tibia and shaft) resulted in a significant increase in AUC for HFRIIs from total hip BMD AUC (nonlinear material model having exponent between 2 and 3, Figure 12).

The performance of two yield stress approximation techniques can be directly compared when they were used with the non-linear material model with an exponent between 1 and

2 [36]. AUCs for HFRI increased when yield stress was estimated from Young's modulus to BMD. In fact, later technique resulted in a significant increase from total hip BMD AUC for trochanteric HFRI. This approach also improved AUCs at shaft ROI for all material models (Figure 11 & Figure 12), probably because samples for yield stress analysis were collected from femoral shaft [91].

Although further study is required to validate above mentioned propositions, however, in the context of this thesis, combining non-linear material model with an exponent between 2 and 3 and yield stress-density relationship into FE model is capable of discriminating more hip fractures than total hip or femoral neck BMD. A number of factors other than material models could be responsible for lower AUCs at femoral neck ROI, which will be discussed in Section 7.1.4.

### 7.1.2 AUCs at critical femur cross-sections

One approach of estimating hip fracture risk was to calculate HFRI at critical femur cross-sections. From Figure 13 it can be seen that none but HFRI at intertrochanteric cross-section had better discriminability than femoral neck BMD. The intertrochanteric cross-section contains weak trabecular bone which is more vulnerable to fracture for a sideways fall. On the contrary, a large proportion of strong cortical bone composes femoral neck and subtrochanteric cross-section. The increase in AUC from femoral neck BMD was significantly higher for intertrochanteric HFRI, however, was not enough to perform as good as total hip BMD. The position of intertrochanteric cross-section depends on the intersecting point of neck-shaft axis and magnitude of the neck-shaft angle. If any rotation (internal/external) in femur occurs during scanning, shaft axis will be inclined towards the

rotational direction. Consequently, the intersecting point will be misplaced, the neck-shaft angle will be fictive, so as intertrochanteric cross-section. This will affect HFRI and in turn discriminability and repeatability at this cross-section. In fact, femur rotation affects positions and HFRI of all critical femur cross-sections to some extent. Figure 18 shows how positions of femur cross-sections can be different for the same patient due to a rotation of the femur. Ideally, the intertrochanteric line should connect lesser and greater trochanter, however, it may not always be possible to detect lesser trochanter in a DXA-image.

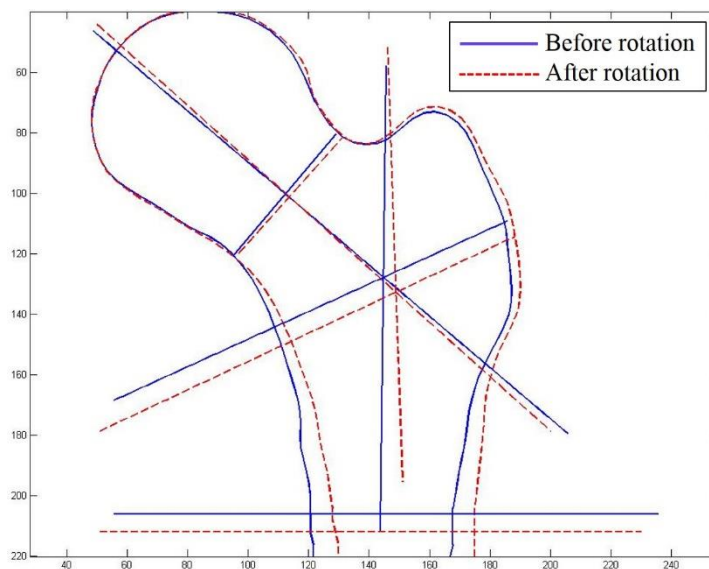


*Figure 18: Effect of femur rotation on position of femur cross-sections*

Similarly, the position of subtrochanteric cross-section depends on the location of the intersecting point of neck-shaft axis. It additionally depends on the width of the narrowest femoral neck. The width varies from subject to subject and in some cases it could be very narrow or wide and impair proper placement of subtrochanteric cross-section. The length of the segmented contour varied from case to case. If the length was very short, the subtrochanteric cross-section might be placed very close to the distal end of the femur (Figure 19). Femur rotation also affects the position of the subtrochanteric cross-section

(Figure 18). Consequently, consistent positioning of the subtrochanteric cross-section with respect to the distal boundary of the femur was not possible to achieve, which might have negatively affected HFRI, hence leading to poor discriminability.

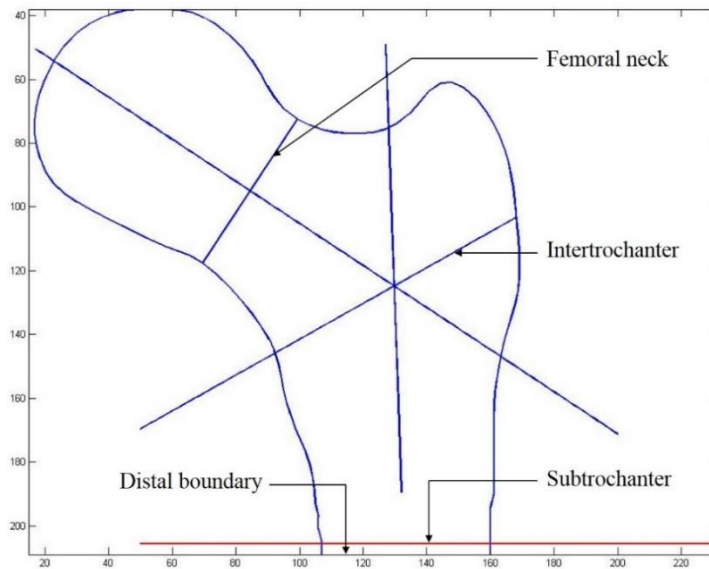


*Figure 19: Positioning of subtrochanteric cross-section close to distal boundary*

The position of femoral neck cross-section depends on the quality of the segmented femur. Although in the present study clinical femoral neck ROI was utilized to detect narrowest neck cross-section, however, poor quality of segmented contour could include non-femoral region and led to misplacement of the narrowest femoral neck. Additionally, its position is affected by femur rotation (Figure 18). The cross-section HFRI were found hypersensitive to the chosen location of cross-sections [33]. Therefore, improper positioning of cross-sections might have caused less than optimal hip fracture discriminability of HFRI. Moreover, the fracture etiology at proximal femur is too complex to be described by a single cross-section. Hence, assessing a region of interest, instead of a cross-section was proposed to minimize the effect associated with proper positioning of the cross-section.

### 7.1.3 AUCs at self-defined ROIs

From Figure 13 it can be seen that the maximum hip fracture discriminability of HFRI increased when we moved from femur cross-section based HFRI calculation technique to ROI based calculation. Interestingly, none of the three 10mm wide ROIs increased AUC from total hip BMD. The self-defined ROIs are rectangles placed around the three critical cross-sections (Figure 6a). As discussed in the previous subsections, consistent positioning of the three critical cross-sections is difficult to achieve. Thus the position of self-defined ROIs is compromised. It is primarily responsible for lower than optimal discriminability of HFRI at three self-defined ROIs.

Alike AUC at the intertrochanteric cross-section, HFRI at intertrochanteric ROI had better discriminability than at femoral neck and subtrochanteric ROI. Intertrochanter is rich in trabecular bone. Using a 10mm wide intertrochanteric ROI means consideration of more trabecular bone in HFRI calculation. As a result, the AUC at this region might have been increased. The position of intertrochanteric ROI depends on similar parameters identical to the intertrochanteric cross-section. Alike Figure 18, Figure 20 shows how the misalignment in shaft axis from femur rotation can affect the position of self-defined intertrochanteric as well as other ROIs. The inconsistent positioning of intertrochanteric ROI from case to case might have caused lower AUC for HFRI than total hip BMD at this region. Compared to intertrochanteric ROI, total ROI is more consistently defined and considers the greatest amount of bone and hence a significant increase in AUC from femoral neck and total BMD can be observed for HFRI at this ROI (Figure 13).

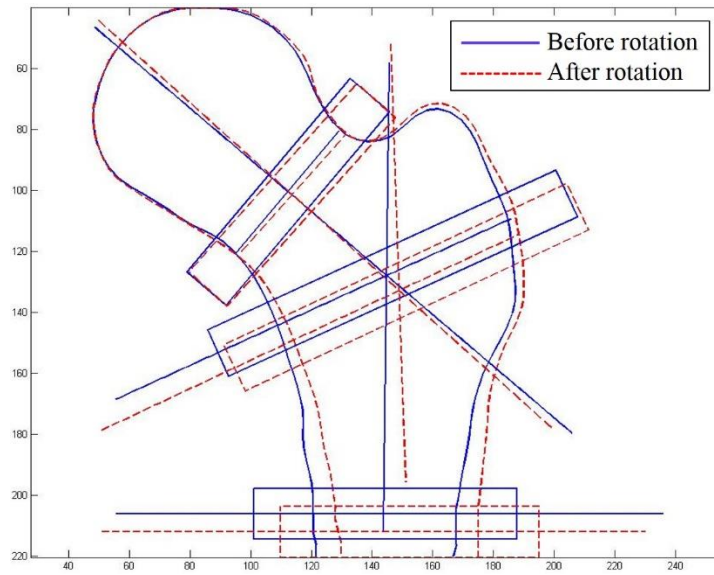


Figure 20: Effect of femur rotation on placement of self-defined ROIs

Consideration of self-defined ROI instead of femur cross-section at femoral neck and subtrochanter also means taking account more trabecular bone in HFRI calculation, since trabecular bone fills in the inner core of the hard cortical shell in those ROIs. However, issues with poor contour quality, as discussed in the previous sub-section for low AUC at femoral neck cross-section, can also be attributed for poor AUC at self-defined and clinical femoral neck ROI which will be elaborated in the next sub-section. Also, AUC at subtrochanteric ROI was lower than that for the subtrochanteric cross-section. As mentioned before, all cases studied here for discriminability had unequal scan length. If the scanned length of the femur was very short, then the subtrochanteric ROI could be placed very close or coincide with the boundary condition applied at the distal end of the femur (Figure 21). If so, HFRI calculated at subtrochanteric ROI would be fictitious. This fact along with femur rotation could be responsible for lower discriminability at subtrochanteric ROI. Maintaining a consistent scan length may resolve the issue.

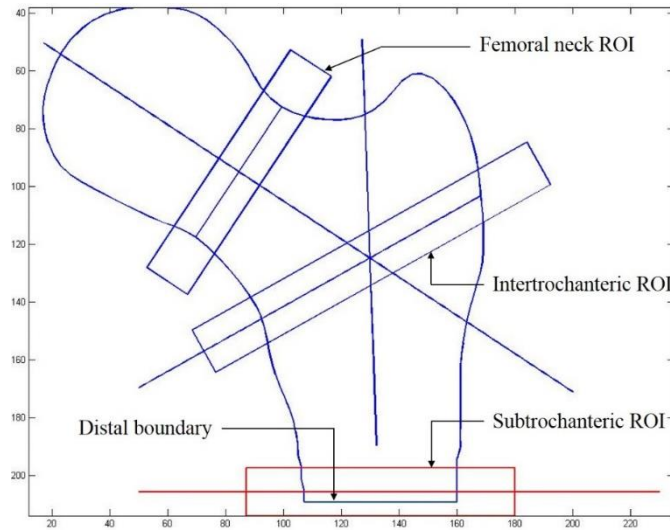


Figure 21: Position of subtrochanteric ROI in a short femur

The ROIs defined by DXA-scanner are more consistently defined and larger in size than self-defined ROIs (Figure 6). Therefore, using DXA-scanner defined (clinical) ROIs is a practical choice towards increasing hip fracture discriminability of the risk indices.

#### 7.1.4 AUCs at clinical ROIs

Hip fracture discriminability increased when HRFIs were calculated at clinical ROIs instead of self-defined ROIs (Figure 13). A significant increase in AUC from femoral neck BMD was observed at all ROIs excluding femoral neck ROI. Improper segmentation of proximal femur could have resulted in poor performance of femoral neck HFRI. At segmentation stage, while interpolating missing points between the femoral head and shaft outline, non-femoral segments might have been included or femoral segment might have been excluded (Figure 22). It could have resulted in improper material property assignment in finite element model. In turn, HRFIs and AUCs might have been affected at femoral neck ROI (both self-defined and clinical ROI). Additionally, as discussed in Section 7.1.1,

after testing different material models, the final material model chosen for HFRI calculation was developed from specimens collected from proximal tibia and shaft. Substantial variation in trabecular bone Young's modulus and yield stress was found across different anatomical sites [94]. Therefore, the final material model used for hip fracture discriminability study may not be a well representative of bone mechanical properties at the femoral neck region.

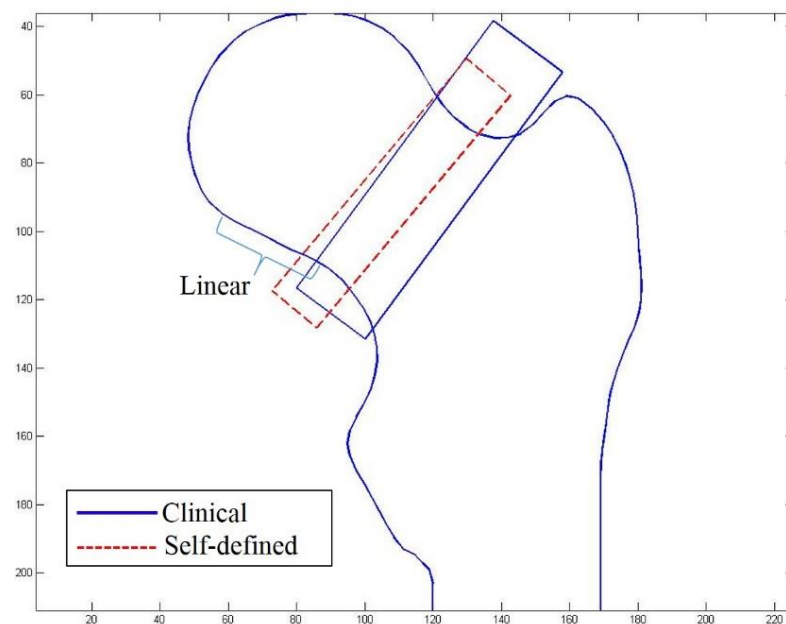


*Figure 22: Relative positions of clinical and self-defined femoral neck ROI and linearly interpolated portion in segmented contour*

Although clinical femoral shaft ROI is now well positioned in the femur, however, issues with scan length prevailed. The shorter length of a scanned femur will restrict consistent positioning of shaft ROI with respect to the distal end of the proximal femur. In other words, the positioning of shaft ROI is partially resolved, hence HFRI at this ROI showed improved discriminability than self-defined subtrochanteric ROI. Figure 23a shows the good positioning of clinical shaft ROI although self-defined subtrochanteric ROI was very

close to the distal boundary. Figure 23b shows the poor positioning of self-defined subtrochanteric and clinical shaft ROI due to the short length of the femur.

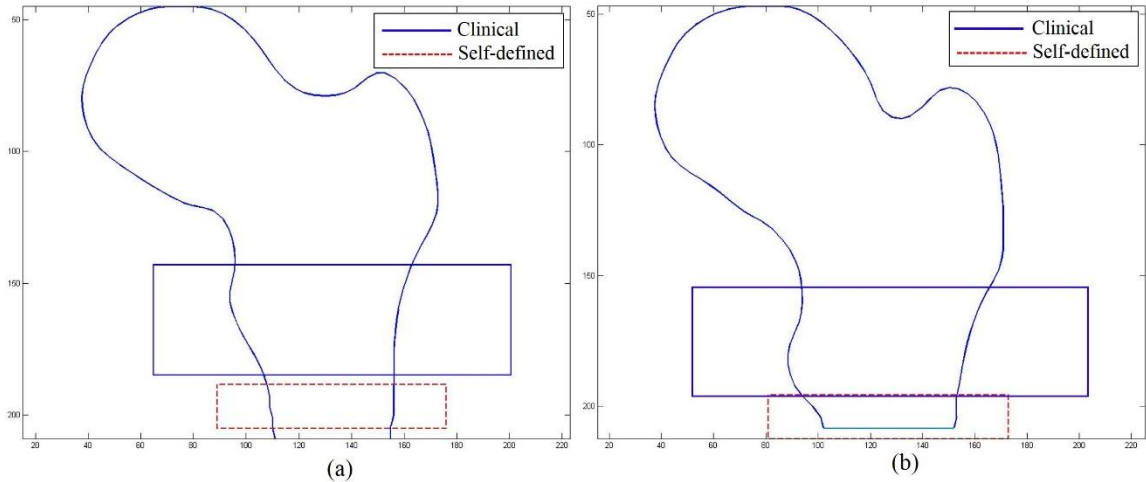


*Figure 23: Relative positions of self-defined subtrochanteric ROI and clinical shaft ROI while scan length was (a) normal (b) short*

A significant increase in AUC from total hip BMD has been achieved for HFRI at clinical trochanteric and total ROI. Sideways impact happens on the greater trochanter and inevitably produces higher stresses on adjacent weak trabecular bones. From a mechanical point of view, the sideways impact will cause stress concentration at the lateral junction of the greater trochanter and femoral neck due to a sharp change in geometry at that location. Clinical trochanteric and total ROI covers greater trochanter and a weak lateral portion of the femoral neck. It implies, they are capable of considering more prospective fracture sites than any other ROI. Since clinical trochanteric ROI is defined by the scanner, so its position is independent of any derived parameter, unlike self-defined intertrochanteric ROI. From the above analysis, it appears that clinical trochanteric ROI or total ROI (both self-defined and clinical) is the appropriate site for fracture analysis.

In agreement to the index of fracture risk (IFR) estimated from DXA-based FE model for different ROIs, as reported by Yang et al. [27], we found the highest AUC of HFRI at the

clinical trochanteric ROI, followed by total and femoral neck ROI. The local HFRI defined in the present study have not been tested before for hip fracture discriminability. A global fracture index, load-to-strength ratio, derived from DXA-based FE model increased AUC marginally from the femoral neck BMD [38]. The total (both clinical and self-defined) and trochanteric HFRI defined in the present study considers a substantial portion of the femur, therefore can be considered as a good representative of global risk index. The AUC of our HFRI calculated at those ROIs were significantly higher than the femoral neck and total hip BMD. Other DXA-based method such as femur strength parameters estimated from HSA did not significantly improve AUC for fracture prediction from femoral neck or total BMD [26, 28]. Obviously, HFRI calculated by our proposed automatic DXA-based FE tool is capable of separating more hip fracture patients from the normal group than any other densitometric or DXA-based methods.

## 7.2 Assessment of correlation analysis

Although AUCs at total ROI (both self-defined and clinical) and clinical trochanteric ROI were comparable in magnitude, however, clinical ROIs are more consistently defined and positioned than self-defined ROIs. Therefore, correlation analysis was performed at clinical ROIs. It can be noticed that HFRI is highly associated with areal BMD at trochanteric ( $R=0.827$ ) and total region ( $R=0.826$ ) than at femoral neck region ( $R=0.772$ ). According to Cheng et al. [114], a significantly better correlation between femoral strength and DXA-derived BMD was observed at trochanteric ( $R^2=0.88$ ) and total ( $R^2=0.76$ ) region than at the femoral neck ( $R^2=0.71$ ) region. Lang et al. [115] also found the strong dependency of femoral strength on trochanteric BMD ( $R^2=0.87$ ) which implies,

trochanteric bone mineral density is mostly responsible for trochanteric fracture. Strong correlation between shaft HFRI and areal BMD suggests that areal BMD at shaft region is more closely related to shaft strength. Turning to the magnitude of mean HFRI at clinical ROIs (Figure 16), it showed a similar pattern to the HFRI calculated by Luo et al. [33]. The femoral neck is enriched with strong cortical bone, however, due to its concave geometry, effective stress would be higher in this region, so as the magnitude of HFRI. Higher mean HFRI at trochanteric region could be due to the abundance of weak trabecular bone in this region [116, 117]. Since total ROI is a composite ROI, therefore mean HFRI at this region had intermediate value. Strong cortical bone at femoral shaft ROI caused lowest mean HFRI at this ROI.

Areal BMD at clinical ROI was estimated from the DXA-BMD file provided by the medicine school using in-house MATLAB codes. True BMDs of 197 cases as calculated by DXA-scanner was known. In-house calculated areal BMDs showed very strong positive correlation with true areal BMDs (Figure 15). It justifies our in-house method of BMD calculation. An accurate estimation of bone mineral density is important since bone material properties were estimated from it and a non-linear relationship between BMD and material properties was assumed finally.

## 7.3 Assessment of short-term repeatability results

Promising short-term repeatability of the proposed automatic DXA-based FE tool derived HFRI was found (Table 5). The scope of CVs in HFRI was from 3% ~ 3.5%, excluding

femoral shaft HFRI. For the requirement of the clinical application, the CVs should be within 2% ~ 3% [112]. The main reason behind less than optimal short-term repeatability of HFRI is rooted in the quality of the segmented femurs and factors external to finite element analysis, as identified by Luo et al. [37]. However, the pattern observed for the short-term repeatability of HFRI of 108 cases agreed to what was found by Luo et al. [37] for all cases, i.e. highest at the total ROI followed by intertrochanteric, femoral neck and subtrochanteric region. A careful review of Table 6 demonstrates an identical pattern of areal BMDs for 108 cases, except at femoral shaft ROI. Maggio et al. [118] also found highest short-term reproducibility for total hip BMD followed by intertrochanteric and femoral neck BMD. Previous research on short-term repeatability of BMDs reported a typical variation between 1-3% [119-121]. The precision of areal BMDs reported in this thesis were less than 2% (Table 6).

Local variation in effective stress originating from the inconsistency of shaft boundary condition in repeat scans could be responsible for poor short-term repeatability of shaft HFRI. Inconsistent finite element boundary condition with respect to shaft ROI was possible if the length of the segmented femur in repeat scans were unequal. To minimize this effect, longer femurs were truncated at the distal end by an amount equal to the difference in length between paired segmented femurs. Yet, short-term repeatability was poor. If the femur was too short (Figure 23b), HFRI at shaft ROI would be changed, as discussed before and it will negatively affect repeatability.

Rotation of femur in repeat scan can also contribute to poor repeatability, especially at trochanteric and shaft region. If the femur is rotated about its head during repeat scans, from Figure 17 (case 8-10) it can be seen that these two ROIs do not rotate with femur

rotation and hence the femur region inside the ROIs will be different. Consequently, HFRI from repeat scans would significantly differ from each other since HFRI is a function of location. The definition of total ROI makes HFRI at this region to be least affected by femur rotation.

Luo et al. [37] identified inconsistent subject positioning and manual segmentation of proximal femur as important sources introducing significant variability in the HFRI. Although the segmentation stage was automated in this study, however, the quality of the segmented femur was not graded and cases may contain high, moderate and low-quality contours. As defined by Luo et al [37], Figure 17 shows samples of moderate and poor quality contours which were included in repeatability analysis with 108 paired scans. After removing such cases, short-term repeatability of HFRI was improved (Table 5). Apart from inconsistent subject positioning during repeat scan [37], poor quality in segmented contour may arise from linear interpolation performed at automatic segmentation stage. Since linear interpolation was done in regions close to the narrowest femoral neck, therefore, poor quality of segmented femur will negatively affect AUC and repeatability at femoral neck ROI. Figure 17 (case 3, 4) shows the difference in contour in paired scans originating from linear interpolation.

The inconsistent positioning of ROIs in repeat scans can also be responsible for large differences in paired HFRI. From Figure 17 it can be seen that positions of all ROIs are not consistent throughout the repeat scans. For case 1-7, it seems ROI positions were adapting with femur rotation and/or subject motion, however, for case 8-10, their positions did not respond to femur rotation. An algorithm may be developed to detect any rotation

in repeat scan and adjust ROI positions accordingly so that identical region in the femur is considered in paired image for HFRI calculation.

Nineteen of the studied subjects were  $\geq 65$  years of age. Although the association between older age and BMD precision error is a matter of dispute [118, 122, 123], however, older age obviously impose difficulty in achieving proper positioning of patients during scanning. A quarter of our studied cases were obese and obesity was found adversely affecting the precision of BMD [121]. The length of the interval between repeat scan was also found affecting the repeatability of BMD [123]. Same day scan-pairs had lower precision error when compared to different day scan pairs. All the repeat scans used in the current study were not acquired on the same day of the first scan. Factors responsible for the precision error in BMD are also responsible for the precision error in HFRI because it is a function of BMD. BMD can be measured directly from DXA scanner as a single parameter, therefore, a very high precision is achievable. On the contrary, HFRI depends on many parameters including BMD and material properties have been derived from BMD using an empirical non-linear equation. Therefore, a small variation in BMD could cause a large precision error in the derived HFRI. This fact is supported by greater improvement in repeatability for HFRI than areal BMDs (Table 5 and Table 6) when thirty paired scans were removed from the precision analysis.

In our study, before removing bad cases, highest repeatability and discriminability of HFRI were found at the clinical total and trochanteric ROI and therefore these two sites should be used for hip fracture risk assessment. Maggio et al. [118] also recommended these two sites for densitometric measurements as reproducibility was higher there. After removing cases responsible for large difference in HFRI, the scope of repeatability for

HFRI were less than 3% (excluding at shaft ROI). These are within clinically acceptable range and hence large scale clinical evaluation of HFRI can be done. Prior to that, an automatic algorithm to detect poor contour quality should be developed and poor contours removed from the analysis.

# Chapter 8

## Conclusions and future work

Hip fracture occurrence rate is increasing and causing immense healthcare cost worldwide. Accurate diagnosis of patients at higher risk of fracture will assist clinicians to plan proper treatment tailored to reduce fracture risk. Additionally, preventive measures against hip fracture will reduce hospital admission from hip fracture and thus reducing healthcare cost. Current methods of diagnosis ignore the mechanical aspects of bone fracture which limits their performance. Image-based finite element methods consider architectural and mechanical aspects of bone to assess its strength. QCT-scans are harmful to patients and QCT-based FEA demands higher computational time. DXA-scans are safe and DXA-based FEA is fast. To make DXA-based FE method clinically acceptable, automation of the process is required. In this reported research, the purpose was to automate the DXA-based finite element procedure and assess accuracy and precision of HFRIIs derived from it. Hip fracture discriminability of the femoral neck and total hip BMD were used as a baseline for evaluating the accuracy of HFRIIs in discriminating hip fracture. Two approaches of HFRI calculation and two definitions of ROI were compared to determine the best approach and definition of ROI for fracture analysis.

## 8.1 Conclusions and contributions

DXA-based finite element methods previously developed were mostly semiautomatic, hence unlikely to be implemented in clinics. The procedure usually involved manual thresholding and/or operator input to segment proximal femur from the hip. It is tedious when thousands of cases need to be processed. Moreover, HFRIIs calculated from previous DXA-based FE model was not assessed for hip fracture discriminability. Based on those research gaps, the major conclusions and contributions of the present study can be expressed as follows:

- The segmentation stage has been made fully automatic. Using manufacturer defined regions of interest, femur outline was extracted from DXA-image automatically. Finite element mesh was generated from the contour coordinates. Triangular elements were used to make the FE model fast and inhomogeneous material properties were assigned at element Gaussian points to capture variability in bone material properties more precisely.
- Bone material properties were estimated from ash density instead of areal BMD. The femur was considered as a plate and the uniform subject-specific thickness of the plate was defined as a function of the narrowest femoral neck width. Pixel-by-pixel ash density was derived from BMD map of DXA-image. Subject-specific body height and weight were incorporated in the FE model to define subject-specific impact load for a sideways fall.
- Detection of critical femur cross-sections was made automatic. Self-defined ROIs were 10mm wide rectangular regions placed around critical femur cross-sections.

Clinical ROIs were directly extracted from 'enCORE' file. HFRI were calculated at critical femur cross-sections, self-defined and clinical ROIs.

- Several material models were tested in the FE tool and it was found that material models had a significant impact on the hip fracture discriminability for HFRI. Dissimilarity in harvesting site, specimen shape, mechanical testing protocol all contributed to the performance of FE tool derived HFRI.
- Hip fracture discriminability of HFRI was assessed by the area under the receiver-operating-characteristics curve (AUC). Discriminability at critical femur cross-sections was lower than reference AUC for total hip BMD. The inconsistent positioning of the critical cross-sections arising from femur rotation and short scan length are the main reasons for poor discriminability. Additionally, a single cross-section is insufficient to approximate fracture behavior of inhomogeneous femur bone. Discriminability increased when HFRI were calculated at ROIs instead of cross-sections, however, issues associated with femur rotation and scan length remained. These issues were partially resolved when HFRI were calculated at larger ROIs. None but self-defined total ROI had significantly higher AUC than that for total BMD. A similar increase in AUC was observed when HFRI were calculated at clinical trochanteric and total ROI. It suggests, considering more femur area in fracture risk calculation improves discrimination accuracy of risk indices. In comparison to risk index developed by other researchers [38], our HFRI improved AUC significantly from femoral neck and total hip BMD.
- The precision of HFRI was encouraging especially when calculated at clinical total ROI. Although short-term repeatability of HFRI was lower than that for areal

BMDs, however, it is reasonable since HFRI is a derived parameter from BMD. The precision of HFRI is mostly affected by segmented contour quality, consistency in ROI positioning and factors external to finite element analysis such as inconsistent patient positioning and scan quality.

Based on the discriminability and precision of HFRI, the ROI-based approach of HFRI calculation and definition of large clinical ROIs have higher potency towards improving hip fracture risk assessment when automatic DXA-based FE tool is used.

## 8.2 Limitations of the present study

Although a comparatively good hip fracture discrimination accuracy and precision have been achieved by HFRI calculated from automatic DXA-based FE tool, few limitations are associated with the present study as discussed below:

- At automatic segmentation stage, while interpolating points between head and shaft outline, points not belonging to femur might be included. Linear interpolation was used for simplicity and computational efficiency. Another way could be to trace femoral portion between head and shaft outline and missing points interpolated using a spline, however, very high quality of DXA-image is a prerequisite for it.
- The amount of error in HFRI calculation contributed by linear interpolation at segmentation stage was not quantified. A DXA-image can be segmented manually as well as automatically and HFRI recalculated to measure the differences.
- The risk of fall i.e. type of fall and probability of fall for the clinical cases was not available since the incident of fall is purely accidental. The FE model was simulated

for most prevent type of fall (sideways fall) responsible for hip fracture and the impact force was estimated by empirical equation. In actual, fall direction, the site of impact, environmental factors, anthropometric characteristics, all affect the impact force experienced from a fall [20]. Therefore, the estimated impact force may not be the one actually experienced in a real scenario. *In vivo* validation of FE-derived HFRI with clinical fracture cases would be challenging because clinical fracture cases are representative of real-world fracture.

- Repeatability of HFRI was not within clinically acceptable range. The quality of segmented contours impacts repeatability of risk indices. High-quality contours will improve repeatability of HFRI. The methodology developed by Luo et al. [37] can be implemented to evaluate contour quality in repeat scans and segmented contours may be graded as high, moderate or low based on the overlapped area in repeat scans. Inconsistency in ROI positions also affected the repeatability of HFRI. An algorithm may be developed which will adapt ROI positions with femur rotation consistently.
- DXA-scans were taken at the left femur and the code developed here can calculate HFRI for left femur only. However, if the scan is taken at the right femur, a few modifications in the code including mirroring the DXA-image will enable to calculate HFRI for the right femur.

Some inherent limitations are associated with the proposed tool. DXA images are projected images and cannot differentiate between cortical and trabecular bone. Bone anisotropy information is absent and material properties can only be modeled in the anteroposterior direction. Impact force is limited to components in the coronal plane. The linear elastic

analysis was done ignoring the post-yield behavior of the bone in accordance with the findings of Juszczak et al. [90].

## 8.3 Future work

Osteoporosis is the process of bone loss with growing age. Due to osteoporosis, bone gets weak and becomes more vulnerable to fracture. Hip fracture is the second most frequent type of osteoporotic fracture while consuming the highest amount of annual healthcare cost. Accidental fall in conjunction with weak bone is the most critical condition to develop hip fracture in elderly. The number of hip fracture is increasing with prolonged life expectancy. Therefore, it is high time to develop a more accurate clinically applicable tool for assessing osteoporotic hip fracture risk. An automatic DXA-based FE tool was developed here to assess osteoporotic hip fracture risk. Compared to BMD, a significant increase in the hip fracture discrimination accuracy was obtained with the HFRI calculated by the automatic tool. Promising short-term repeatability of HFRI was observed with further provision for improvement. Nevertheless, with the current level of accuracy and precision, the proposed tool can be used for large scale clinical evaluation of HFRI. Prospective future works should be tailored to large-scale clinical evaluation and minimization of limitations mentioned above. Additional future works may include:

- A general guideline can be developed to maintain consistent patient positioning for scanning. Besides, scan length should be such long so that segmented femur can hold all ROIs especially shaft ROI.

- Failure load for the femur is influenced by the direction of fall [124]. In this study, impact force has been applied in pressure form on the greater trochanter. The direction of applied load can be changed to quantify its influence on HFRI.
- The proposed automatic DXA-based FE tool can be used for longitudinal monitoring of hip fracture risk and effect of a therapy. When HFRI for consecutive ages of a patient is available, data can be analyzed to identify the trend and extrapolated to predict 10 years hip fracture chances.
- A user-friendly interface similar to FRAX-tool can be developed where the physician or patient has to upload DXA-image and HFRI will be displayed subsequently.
- An automatic algorithm to assess scan quality prior to finite element analysis can be developed. Based on quality, poor quality contours should not be processed.

DXA-based FE tool developed here is automatic, fast, accurate, cost-effective and non-invasive. After large scale clinical evaluation, the tool can be adopted in the clinics for assessing hip fracture risk. A successful implementation of the tool will enable physicians to identify high-risk patients and plan preventive measures which will truncate annual burden of hip fracture-related healthcare cost.

# Bibliography

- [1] E. Barrett-Connor, “The economic and human costs of osteoporotic fracture,” *The American Journal of Medicine*, vol. 98, no. 2, pp. 3S–8S, 1995.
- [2] C. Cooper, E. J. Atkinson, S. J. Jacobsen, W. M. O’Fallon, and L. J. Melton, “Population-based study of survival after osteoporotic fractures,” *American Journal of Epidemiology*, vol. 137, no. 9, pp. 1001–1005, 1993.
- [3] S. R. Cummings, D. B. Karpf, F. Harris, H. K. Genant, K. Ensrud, A. Z. LaCroix, and D. M. Black, “Improvement in spine bone density and reduction in risk of vertebral fractures during treatment with antiresorptive drugs,” *The American Journal of Medicine*, vol. 112, no. 4, pp. 281–289, 2002.
- [4] O. Johnell and J. Kanis, “An estimate of the worldwide prevalence and disability associated with osteoporotic fractures,” *Osteoporosis International*, vol. 17, no. 12, pp. 1726–1733, 2006.
- [5] C. Cooper, G. Campion, and L. Melton Iii, “Hip fractures in the elderly: a world-wide projection,” *Osteoporosis International*, vol. 2, no. 6, pp. 285–289, 1992.

- [6] R. Burge, B. Dawson-Hughes, D. H. Solomon, J. B. Wong, A. King, and A. Tosteson, "Incidence and economic burden of osteoporosis-related fractures in the United States, 2005–2025," *Journal of Bone and Mineral Research*, vol. 22, no. 3, pp. 465–475, 2007.
- [7] E. A. Papadimitropoulos, P. C. Coyte, R. G. Josse, and C. E. Greenwood, "Current and projected rates of hip fracture in Canada," *Canadian Medical Association Journal*, vol. 157, no. 10, pp. 1357–1363, 1997.
- [8] M. Wiktorowicz, R. Goeree, A. Papaioannou, J. D. Adachi, and E. Papadimitropoulos, "Economic implications of hip fracture: health service use, institutional care and cost in Canada," *Osteoporosis International*, vol. 12, no. 4, pp. 271–278, 2001.
- [9] J. A. Kanis, E. V. McCloskey, H. Johansson, A. Oden, L. J. Melton, and N. Khaltsev, "A reference standard for the description of osteoporosis," *Bone*, vol. 42, no. 3, pp. 467–475, 2008.
- [10] D. Marshall, O. Johnell, and H. Wedel, "Meta-analysis of how well measures of bone mineral density predict occurrence of osteoporotic fractures," *British Medical Journal*, vol. 312, no. 7041, pp. 1254–1259, 1996.
- [11] S. Schuit, M. Van der Klift, A. Weel, C. De Laet, H. Burger, E. Seeman, A. Hofman, A. Uitterlinden, J. Van Leeuwen, and H. Pols, "Fracture incidence and association with bone mineral density in elderly men and women: the rotterdam study," *Bone*, vol. 34, no. 1, pp. 195–202, 2004.
- [12] S. A. Wainwright, L. M. Marshall, K. E. Ensrud, J. A. Cauley, D. M. Black, T. A. Hillier, M. C. Hochberg, M. T. Vogt, and E. S. Orwoll, "Hip fracture in women without osteoporosis," *The Journal of Clinical Endocrinology & Metabolism*, vol. 90, no. 5, pp. 2787–2793, 2005.

- [13] T. Dufresne, P. Chmielewski, M. Manhart, T. Johnson, and B. Borah, "Risedronate preserves bone architecture in early postmenopausal women in 1 year as measured by three-dimensional microcomputed tomography," *Calcified Tissue International*, vol. 73, no. 5, pp. 423–432, 2003.
- [14] S. R. Cummings and L. J. Melton, "Epidemiology and outcomes of osteoporotic fractures," *The Lancet*, vol. 359, no. 9319, pp. 1761–1767, 2002.
- [15] E.-M. Lochmüller, J.-B. Zeller, D. Kaiser, F. Eckstein, J. Landgraf, R. Putz, and R. Steldinger, "Correlation of femoral and lumbar DXA and calcaneal ultrasound, measured *in situ* with intact soft tissues, with the *in vitro* failure loads of the proximal femur," *Osteoporosis International*, vol. 8, no. 6, pp. 591–598, 1998.
- [16] L. J. Melton, E. A. Chrischilles, C. Cooper, A. W. Lane, and B. L. Riggs, "How many women have osteoporosis?" *Journal of Bone and Mineral Research*, vol. 20, no. 5, pp. 886–892, 2005.
- [17] D. Testi, M. Viceconti, F. Baruffaldi, and A. Cappello, "Risk of fracture in elderly patients: a new predictive index based on bone mineral density and finite element analysis," *Computer Methods and Programs in Biomedicine*, vol. 60, no. 1, pp. 23–33, 1999.
- [18] E. Seeman and P. D. Delmas, "Bone quality - the material and structural basis of bone strength and fragility," *New England Journal of Medicine*, vol. 354, no. 21, pp. 2250–2261, 2006.
- [19] P. Pulkkinen, C.-C. Glüer, and T. Jämsä, "Investigation of differences between hip fracture types: a worthy strategy for improved risk assessment and fracture prevention," *Bone*, vol. 49, no. 4, pp. 600–604, 2011.

- [20] Y. Luo, “A biomechanical sorting of clinical risk factors affecting osteoporotic hip fracture,” *Osteoporosis International*, pp. 1–17, 2015.
- [21] J. A. Kanis, A. Oden, H. Johansson, F. Borgström, O. Ström, and E. McCloskey, “FRAX and its applications to clinical practice,” *Bone*, vol. 44, no. 5, pp. 734–743, 2009.
- [22] K. G. Faulkner, S. R. Cummings, D. Black, L. Palermo, C.-C. Glüer, and H. K. Genant, “Simple measurement of femoral geometry predicts hip fracture: the study of osteoporotic fractures,” *Journal of Bone and Mineral Research*, vol. 8, no. 10, pp. 1211–1217, 1993.
- [23] M. Peacock, C. Turner, G. Liu, A. Manatunga, L. Timmerman, and C. Johnston Jr, “Better discrimination of hip fracture using bone density, geometry and architecture,” *Osteoporosis International*, vol. 5, no. 3, pp. 167–173, 1995.
- [24] K. M. Karlsson, I. Sernbo, K. J. Obrant, I. Redlund-Johnell, and O. Johnell, “Femoral neck geometry and radiographic signs of osteoporosis as predictors of hip fracture,” *Bone*, vol. 18, no. 4, pp. 327–330, 1996.
- [25] C. Bergot, V. Bousson, A. Meunier, M. Laval-Jeantet, and J. Laredo, “Hip fracture risk and proximal femur geometry from DXA scans,” *Osteoporosis International*, vol. 13, no. 7, pp. 542–550, 2002.
- [26] W. Leslie, P. Pahlavan, J. Tsang, L. Lix, M. B. D. Program *et al.*, “Prediction of hip and other osteoporotic fractures from hip geometry in a large clinical cohort,” *Osteoporosis International*, vol. 20, no. 10, pp. 1767–1774, 2009.
- [27] L. Yang, N. Peel, J. A. Clowes, E. V. McCloskey, and R. Eastell, “Use of DXA-based structural engineering models of the proximal femur to discriminate hip fracture,” *Journal of Bone and Mineral Research*, vol. 24, no. 1, pp. 33–42, 2009.

- [28] F. A. Mourtada, T. J. Beck, D. L. Hauser, C. B. Ruff, and G. Bao, "Curved beam model of the proximal femur for estimating stress using dual-energy X-ray absorptiometry derived structural geometry," *Journal of Orthopaedic Research*, vol. 14, no. 3, pp. 483–492, 1996.
- [29] L. Yang, E. McCloskey, and R. Eastell, "A DXA-based composite beam model of the proximal femur for stress estimation," *Journal of Bone and Mineral Research*, vol. 21, no. 7., pp. 1161–1161, 2006.
- [30] N. Crabtree, H. Kroger, A. Martin, H. Pols, R. Lorenc, J. Nijs, J. Stepan, J. Falch, T. Miazgowski, S. Grazio *et al.*, "Improving risk assessment: hip geometry, bone mineral distribution and bone strength in hip fracture cases and controls. The EPOS study," *Osteoporosis International*, vol. 13, no. 1, pp. 48–54, 2002.
- [31] K. G. Faulkner, W. Wacker, H. Barden, C. Simonelli, P. Burke, S. Ragi, and L. Del Rio, "Femur strength index predicts hip fracture independent of bone density and hip axis length," *Osteoporosis International*, vol. 17, no. 4, pp. 593–599, 2006.
- [32] S. Kaptoge, T. J. Beck, J. Reeve, K. L. Stone, T. A. Hillier, J. A. Cauley, and S. R. Cummings, "Prediction of incident hip fracture risk by femur geometry variables measured by hip structural analysis in the study of osteoporotic fractures," *Journal of Bone and Mineral Research*, vol. 23, no. 12, pp. 1892–1904, 2008.
- [33] Y. Luo, Z. Ferdous, and W. Leslie, "A preliminary dual-energy X-ray absorptiometry-based finite element model for assessing osteoporotic hip fracture risk," *Proceedings of the Institution of Mechanical Engineers, Part H: Journal of Engineering in Medicine*, vol. 225, pp. 1188-1195, 2011.

- [34] J. Lotz, E. Cheal, and W. Hayes, "Fracture prediction for the proximal femur using finite element models: part I—linear analysis," *Journal of Biomechanical Engineering*, vol. 113, no. 4, pp. 353–360, 1991.
- [35] J. H. Keyak, S. A. Rossi, K. A. Jones, and H. B. Skinner, "Prediction of femoral fracture load using automated finite element modeling," *Journal of Biomechanics*, vol. 31, no. 2, pp. 125–133, 1997.
- [36] J. O. Den Buijs and D. Dragomir-Daescu, "Validated finite element models of the proximal femur using two-dimensional projected geometry and bone density," *Computer Methods and Programs in Biomedicine*, vol. 104, no. 2, pp. 168–174, 2011.
- [37] Y. Luo, Z. Ferdous, and W. D. Leslie, "Precision study of DXA-based patient-specific finite element modeling for assessing hip fracture risk," *International Journal for Numerical Methods in Biomedical Engineering*, vol. 29, no. 5, pp. 615–629, 2013.
- [38] K. E. Naylor, E. V. McCloskey, R. Eastell, and L. Yang, "Use of DXA-based finite element analysis of the proximal femur in a longitudinal study of hip fracture," *Journal of Bone and Mineral Research*, vol. 28, no. 5, pp. 1014–1021, 2013.
- [39] L. Yang, L. Palermo, D. M. Black, and R. Eastell, "Prediction of incident hip fracture with the estimated femoral strength by finite element analysis of DXA scans in the study of osteoporotic fractures," *Journal of Bone and Mineral Research*, vol. 29, no. 12, pp. 2594–2600, 2014.
- [40] D. D. Cody, G. J. Gross, F. J. Hou, H. J. Spencer, S. A. Goldstein, and D. P. Fyhrie, "Femoral strength is better predicted by finite element models than QCT and DXA," *Journal of Biomechanics*, vol. 32, no. 10, pp. 1013–1020, 1999.

- [41] E. S. Orwoll, L. M. Marshall, C. M. Nielson, S. R. Cummings, J. Lapidus, J. A. Cauley, K. Ensrud, N. Lane, P. R. Hoffmann, D. L. Kopperdahl *et al.*, “Finite element analysis of the proximal femur and hip fracture risk in older men,” *Journal of Bone and Mineral Research*, vol. 24, no. 3, pp. 475–483, 2009.
- [42] C. Langton, S. Pisharody, and J. Keyak, “Comparison of 3D finite element analysis derived stiffness and BMD to determine the failure load of the excised proximal femur,” *Medical Engineering & Physics*, vol. 31, no. 6, pp. 668–672, 2009.
- [43] R. Bouillon, P. Burckhardt, C. Christiansen, H. Fleisch, T. Fujita, C. Gennari, T. Marin, G. Mazzuoli, L. Melton, J. Ringe *et al.*, “Consensus development conference: prophylaxis and treatment of osteoporosis,” *American Journal of Medicine*, vol. 90, pp. 107–110, 1991.
- [44] S. L. Hui, C. W. Slemenda, and C. C. Johnston Jr, “Age and bone mass as predictors of fracture in a prospective study.” *Journal of Clinical Investigation*, vol. 81, no. 6, p. 1804, 1988.
- [45] R. D. Wasnich, P. D. Ross, L. K. Heilbrun, and J. M. Vogel, “Selection of the optimal skeletal site for fracture risk prediction.” *Clinical Orthopaedics and Related Research*, no. 216, pp. 262–269, 1987.
- [46] P. D. Ross, R. D. Wasnich, and J. M. Vogel, “Detection of prefracture spinal osteoporosis using bone mineral absorptiometry,” *Journal of Bone and Mineral Research*, vol. 3, no. 1, pp. 1–11, 1988.
- [47] P. Gärdsell, O. Johnell, and B. E. Nilsson, “The predictive value of bone loss for fragility fractures in women: a longitudinal study over 15 years,” *Calcified Tissue International*, vol. 49, no. 2, pp. 90–94, 1991.

- [48] S. R. Cummings, W. Browner, D. Black, M. Nevitt, H. Genant, J. Cauley, K. Ensrud, J. Scott, and T. Vogt, "Bone density at various sites for prediction of hip fractures," *The Lancet*, vol. 341, no. 8837, pp. 72–75, 1993.
- [49] L. J. Melton, E. J. Atkinson, W. M. O'Fallon, H. W. Wahner, and B. L. Riggs, "Long-term fracture prediction by bone mineral assessed at different skeletal sites," *Journal of Bone and Mineral Research*, vol. 8, no. 10, pp. 1227–1233, 1993.
- [50] World Health Organization *et al.*, "Assessment of fracture risk and its application to screening for postmenopausal osteoporosis: report of a WHO study group [meeting held in Rome from 22 to 25 June 1992]," 1994.
- [51] E. S. Leib, E. M. Lewiecki, N. Binkley, and R. C. Hamdy, "Official positions of the international society for clinical densitometry," *Journal of Clinical Densitometry*, vol. 7, no. 1, pp. 1–5, 2004.
- [52] J. A. Kanis, L. J. Melton, C. Christiansen, C. C. Johnston, and N. Khaltsev, "The diagnosis of osteoporosis," *Journal of Bone and Mineral Research*, vol. 9, no. 8, pp. 1137–1141, 1994.
- [53] B. E. Nordin, "The definition and diagnosis of osteoporosis," *Calcified Tissue International*, vol. 40, no. 2, pp. 57–58, 1987.
- [54] J. Kanis, D. Black, C. Cooper, P. Dargent, B. Dawson-Hughes, C. De Laet, P. Delmas, J. Eisman, O. Johnell, B. Jonsson *et al.*, "A new approach to the development of assessment guidelines for osteoporosis," *Osteoporosis International*, vol. 13, no. 7, pp. 527–536, 2002.
- [55] E. S. Siris, P. D. Miller, E. Barrett-Connor, K. G. Faulkner, L. E. Wehren, T. A. Abbott, M. L. Berger, A. C. Santora, and L. M. Sherwood, "Identification and fracture outcomes of undiagnosed low bone mineral density in postmenopausal women: Results

from the national osteoporosis risk assessment,” *Obstetrical & Gynecological Survey*, vol. 57, no. 4, pp. 220–221, 2002.

[56] J. Kanis, O. Johnell, A. Oden, B. Jonsson, C. De Laet, and A. Dawson, “Risk of hip fracture according to the World Health Organization criteria for osteopenia and osteoporosis,” *Bone*, vol. 27, no. 5, pp. 585–590, 2000.

[57] J. A. Kanis, W. H. Organization *et al.*, *Assessment of osteoporosis at the primary health care level*. WHO Collaborating Centre for Metabolic Bone Diseases, University of Sheffield Medical School, 2008.

[58] J. Kanis, I. Barton, and O. Johnell, “Risedronate decreases fracture risk in patients selected solely on the basis of prior vertebral fracture,” *Osteoporosis International*, vol. 16, no. 5, pp. 475–482, 2005.

[59] J. Kanis, A. Odén, O. Johnell, H. Johansson, C. De Laet, J. Brown, P. Burckhardt, C. Cooper, C. Christiansen, S. Cummings *et al.*, “The use of clinical risk factors enhances the performance of BMD in the prediction of hip and osteoporotic fractures in men and women,” *Osteoporosis International*, vol. 18, no. 8, pp. 1033–1046, 2007.

[60] J. A. Kanis, O. Johnell, C. De Laet, B. Jonsson, A. Oden, and A. K. Ogelsby, “International variations in hip fracture probabilities: implications for risk assessment,” *Journal of Bone and Mineral Research*, vol. 17, no. 7, pp. 1237–1244, 2002.

[61] C. Cooper, Z. Cole, C. Holroyd, S. Earl, N. Harvey, E. Dennison, L. Melton, S. Cummings, J. Kanis, I. C. W. G. on Fracture Epidemiology *et al.*, “Secular trends in the incidence of hip and other osteoporotic fractures,” *Osteoporosis International*, vol. 22, no. 5, pp. 1277–1288, 2011.

- [62] J. A. Kanis, D. Hans, C. Cooper, S. Baim, J. P. Bilezikian, N. Binkley, J. A. Cauley, J. Compston, B. Dawson-Hughes, G. E.-H. Fuleihan *et al.*, “Interpretation and use of FRAX in clinical practice,” *Osteoporosis International*, vol. 22, no. 9, pp. 2395–2411, 2011.
- [63] S. L. Silverman and A. D. Calderon, “The utility and limitations of FRAX: a US perspective,” *Current Osteoporosis Reports*, vol. 8, no. 4, pp. 192–197, 2010.
- [64] R. G. Cumming and R. J. Klineberg, “Fall frequency and characteristics and the risk of hip fractures,” *Journal of the American Geriatrics Society*, vol. 42, no. 7, pp. 774–778, 1994.
- [65] M. Nankaku, H. Kanzaki, T. Tsuboyama, and T. Nakamura, “Evaluation of hip fracture risk in relation to fall direction,” *Osteoporosis International*, vol. 16, no. 11, pp. 1315–1320, 2005.
- [66] M. J. Silva, “Biomechanics of osteoporotic fractures,” *Injury*, vol. 38, no. 3, pp. 69–76, 2007.
- [67] S. Pisharody, R. Phillips, and C. Langton, “Sensitivity of proximal femoral stiffness and areal bone mineral density to changes in bone geometry and density,” *Proceedings of the Institution of Mechanical Engineers, Part H: Journal of Engineering in Medicine*, vol. 222, no. 3, pp. 367–375, 2008.
- [68] T. M. Keaveny, D. L. Kopperdahl, L. J. Melton, P. F. Hoffmann, S. Amin, B. L. Riggs, and S. Khosla, “Age-dependence of femoral strength in white women and men,” *Journal of Bone and Mineral Research*, vol. 25, no. 5, pp. 994–1001, 2010.

- [69] J. Lotz, E. Cheal, and W. C. Hayes, "Fracture prediction for the proximal femur using finite element models: part II - nonlinear analysis," *Journal of Biomechanical Engineering*, vol. 113, no. 4, pp. 361–365, 1991.
- [70] J. Keyak, J. Meagher, H. Skinner, and C. Mote, "Automated three-dimensional finite element modelling of bone: a new method," *Journal of Biomedical Engineering*, vol. 12, no. 5, pp. 389–397, 1990.
- [71] J. Lotz, W. Hayes, and T. Gerhart, "The structural contribution of cortical and trabecular bone in the femoral neck," *Transactions of the Orthopedic Research Society*, vol. 13, p. 232, 1988.
- [72] J. Keyak, S. Rossi, K. Jones, C. Les, and H. Skinner, "Prediction of fracture location in the proximal femur using finite element models," *Medical Engineering & Physics*, vol. 23, no. 9, pp. 657–664, 2001.
- [73] J. Keyak, "Improved prediction of proximal femoral fracture load using nonlinear finite element models," *Medical Engineering & Physics*, vol. 23, no. 3, pp. 165–173, 2001.
- [74] J. H. Keyak, T. S. Kaneko, J. Tehranzadeh, and H. B. Skinner, "Predicting proximal femoral strength using structural engineering models." *Clinical Orthopaedics and Related Research*, vol. 437, pp. 219–228, 2005.
- [75] A. Van den Kroonenberg, W. C. Hayes, and T. McMahon, "Dynamic models for sideways falls from standing height," *Journal of Biomechanical Engineering*, vol. 117, no. 3, pp. 309–318, 1995.
- [76] W. E. Barlow, L. Ichikawa, D. Rosner, and S. Izumi, "Analysis of case-cohort designs," *Journal of Clinical Epidemiology*, vol. 52, no. 12, pp. 1165–1172, 1999.

- [77] M. Bessho, I. Ohnishi, T. Matsumoto, S. Ohashi, J. Matsuyama, K. Tobita, M. Kaneko, and K. Nakamura, "Prediction of proximal femur strength using a CT-based nonlinear finite element method: differences in predicted fracture load and site with changing load and boundary conditions," *Bone*, vol. 45, no. 2, pp. 226–231, 2009.
- [78] D. Testi, M. Viceconti, A. Cappello, and S. Gnudi, "Prediction of hip fracture can be significantly improved by a single biomedical indicator," *Annals of Biomedical Engineering*, vol. 30, no. 6, pp. 801–807, 2002.
- [79] J. Thevenot, P. Pulkkinen, J. E. Koivumäki, V. Kuhn, F. Eckstein, and T. Jämsä, "Discrimination of cervical and trochanteric hip fractures using radiography-based two-dimensional finite element models," *Open Bone J*, vol. 1, pp. 16–22, 2009.
- [80] R. Hinton and G. S. Smith, "The association of age, race, and sex with the location of proximal femoral fractures in the elderly." *The Journal of Bone and Joint Surgery. American Volume*, vol. 75, no. 5, pp. 752–759, 1993.
- [81] R. Y. Hinton, D. W. Lennox, F. R. Ebert, S. J. Jacobsen, and G. S. Smith, "Relative rates of fracture of the hip in the United States. Geographic, sex, and age variations." *The Journal of Bone and Joint Surgery*, vol. 77, no. 5, pp. 695–702, 1995.
- [82] J. D. Michelson, A. Myers, R. Jinnah, Q. Cox, and M. Van Natta, "Epidemiology of hip fractures among the elderly: Risk factors for fracture type." *Clinical Orthopaedics and Related Research*, vol. 311, pp. 129–135, 1995.
- [83] M. R. Karagas, G. L. Lu-Yao, J. A. Barrett, M. L. Beach, and J. A. Baron, "Heterogeneity of hip fracture: age, race, sex, and geographic patterns of femoral neck and trochanteric fractures among the us elderly," *American Journal of Epidemiology*, vol. 143, no. 7, pp. 677–682, 1996.

- [84] B. C. Khoo, T. J. Beck, Q.-H. Qiao, P. Parakh, L. Semanick, R. L. Prince, K. P. Singer, and R. I. Price, “In vivo short-term precision of hip structure analysis variables in comparison with bone mineral density using paired dual-energy x-ray absorptiometry scans from multi-center clinical trials,” *Bone*, vol. 37, no. 1, pp. 112–121, 2005.
- [85] S. Van Cauter, M. De Beule, A. Van Haver, P. Verdonk, and B. Verhegghe, “Automated extraction of the femoral shaft axis and its distal entry point from full and reduced 3d models,” in *3rd ECCOMAS Thematic conference on Computational Vision and Medical Image Processing (VipIMAGE 2011)*. Taylor & Francis Group, 2011, pp. 57–61.
- [86] L. Peng, J. Bai, X. Zeng, and Y. Zhou, “Comparison of isotropic and orthotropic material property assignments on femoral finite element models under two loading conditions,” *Medical Engineering & Physics*, vol. 28, no. 3, pp. 227–233, 2006.
- [87] E. Schileo, F. Taddei, L. Cristofolini, and M. Viceconti, “Subject-specific finite element models implementing a maximum principal strain criterion are able to estimate failure risk and fracture location on human femurs tested in vitro,” *Journal of Biomechanics*, vol. 41, no. 2, pp. 356–367, 2008.
- [88] B. Helgason, E. Perilli, E. Schileo, F. Taddei, S. Brynjólfsson, and M. Viceconti, “Mathematical relationships between bone density and mechanical properties: a literature review,” *Clinical Biomechanics*, vol. 23, no. 2, pp. 135–146, 2008.
- [89] F. Linde, I. Hvid, and F. Madsen, “The effect of specimen geometry on the mechanical behaviour of trabecular bone specimens,” *Journal of Biomechanics*, vol. 25, no. 4, pp. 359–368, 1992.

- [90] M. M. Juszczak, L. Cristofolini, and M. Viceconti, "The human proximal femur behaves linearly elastic up to failure under physiological loading conditions," *Journal of Biomechanics*, vol. 44, no. 12, pp. 2259–2266, 2011.
- [91] T. S. Keller, "Predicting the compressive mechanical behavior of bone," *Journal of Biomechanics*, vol. 27, no. 9, pp. 1159–1168, 1994.
- [92] J. C. Lotz, T. N. Gerhart, and W. C. Hayes, "Mechanical properties of metaphyseal bone in the proximal femur," *Journal of Biomechanics*, vol. 24, no. 5, pp. 3173–3253, 1991.
- [93] J. Keyak, I. Lee, and H. Skinner, "Correlations between orthogonal mechanical properties and density of trabecular bone: use of different densitometric measures," *Journal of Biomedical Materials Research*, vol. 28, no. 11, pp. 1329–1336, 1994.
- [94] E. F. Morgan and T. M. Keaveny, "Dependence of yield strain of human trabecular bone on anatomic site," *Journal of Biomechanics*, vol. 34, no. 5, pp. 569–577, 2001.
- [95] E. F. Morgan, H. H. Bayraktar, and T. M. Keaveny, "Trabecular bone modulus–density relationships depend on anatomic site," *Journal of Biomechanics*, vol. 36, no. 7, pp. 897–904, 2003.
- [96] F. Linde and I. Hvid, "The effect of constraint on the mechanical behaviour of trabecular bone specimens," *Journal of Biomechanics*, vol. 22, no. 5, pp. 485–490, 1989.
- [97] B. Li and R. M. Aspden, "Composition and mechanical properties of cancellous bone from the femoral head of patients with osteoporosis or osteoarthritis," *Journal of Bone and Mineral Research*, vol. 12, no. 4, pp. 641–651, 1997.
- [98] Z. Ferdous, "Development of a DXA-based patient-specific finite element model for assessing osteoporotic fracture risk," Master's thesis, University of Manitoba, 2012.

- [99] E. Madenci and I. Guven, *The finite element method and applications in engineering using ANSYS*. Springer, 2015.
- [100] J. A. Grisso, J. L. Kelsey, B. L. Strom, G. Y. Ghiu, G. Maislin, L. A. O'Brien, S. Hoffman, and F. Kaplan, "Risk factors for falls as a cause of hip fracture in women," *New England Journal of Medicine*, vol. 324, no. 19, pp. 1326–1331, 1991.
- [101] S. Robinovitch, W. C. Hayes, and T. McMahon, "Prediction of femoral impact forces in falls on the hip," *Journal of Biomechanical Engineering*, vol. 113, no. 4, pp. 366–374, 1991.
- [102] T. Yoshikawa, C. Turner, M. Peacock, C. Slemenda, C. Weaver, D. Teegarden, P. Markwardt, and D. Burr, "Geometric structure of the femoral neck measured using dual-energy X-ray absorptiometry," *Journal of Bone and Mineral Research*, vol. 9, no. 7, pp. 1053–1064, 1994.
- [103] Y. Luo, M. Nasiri Sarvi, P. Sun, W. D. Leslie, and J. Ouyang, "Prediction of impact force in sideways fall by image-based subject-specific dynamics model," *International Biomechanics*, vol. 1, no. 1, pp. 1–14, 2014.
- [104] A. B. Dufour, B. Roberts, K. E. Broe, D. P. Kiel, M. L. Bouxsein, and M. T. Hannan, "The factor-of-risk biomechanical approach predicts hip fracture in men and women: the Framingham study," *Osteoporosis International*, vol. 23, no. 2, pp. 513–520, 2012.
- [105] T. M. Keaveny and M. L. Bouxsein, "Theoretical implications of the biomechanical fracture threshold," *Journal of Bone and Mineral Research*, vol. 23, no. 10, pp. 1541–1547, 2008.
- [106] E. R. Myers and S. E. Wilson, "Biomechanics of osteoporosis and vertebral fracture," *Spine*, vol. 22, no. 24, pp. 25S–31S, 1997.

- [107] W. C. Hayes, S. Piazza, and P. Zysset, “Biomechanics of fracture risk prediction of the hip and spine by quantitative computed tomography.” *Radiologic Clinics of North America*, vol. 29, no. 1, pp. 1–18, 1991.
- [108] Y. Duan, E. Seeman, and C. H. Turner, “The biomechanical basis of vertebral body fragility in men and women,” *Journal of Bone and Mineral Research*, vol. 16, no. 12, pp. 2276–2283, 2001.
- [109] Y. Duan, F. Duboeuf, F. Munoz, P. D. Delmas, and E. Seeman, “The fracture risk index and bone mineral density as predictors of vertebral structural failure,” *Osteoporosis International*, vol. 17, no. 1, pp. 54–60, 2006.
- [110] J. R. Barber, *Intermediate mechanics of materials*. Springer Science & Business Media, 2010, vol. 175.
- [111] V. D. Da Silva, *Mechanics and strength of materials*. Springer Science & Business Media, 2005.
- [112] C.-C. Glüer, G. Blake, Y. Lu, B. Blunt, M. Jergas, and H. Genant, “Accurate assessment of precision errors: how to measure the reproducibility of bone densitometry techniques,” *Osteoporosis International*, vol. 5, no. 4, pp. 262–270, 1995.
- [113] T. Fawcett, “An introduction to ROC analysis,” *Pattern Recognition Letters*, vol. 27, no. 8, pp. 861–874, 2006.
- [114] X. Cheng, G. Lowet, S. Boonen, P. Nicholson, P. Brys, J. Nijs, and J. Dequeker, “Assessment of the strength of proximal femur in vitro: relationship to femoral bone mineral density and femoral geometry,” *Bone*, vol. 20, no. 3, pp. 213–218, 1997.

- [115] T. Lang, J. Keyak, M. Heitz, P. Augat, Y. Lu, A. Mathur, and H. Genant, "Volumetric quantitative computed tomography of the proximal femur: precision and relation to bone strength," *Bone*, vol. 21, no. 1, pp. 101–108, 1997.
- [116] J. Spadaro, F. Werner, R. Brenner, M. Fortino, L. Fay, and W. Edwards, "Cortical and trabecular bone contribute strength to the osteopenic distal radius," *Journal of Orthopaedic Research*, vol. 12, no. 2, pp. 211–218, 1994.
- [117] H. H. Bayraktar, E. F. Morgan, G. L. Niebur, G. E. Morris, E. K. Wong, and T. M. Keaveny, "Comparison of the elastic and yield properties of human femoral trabecular and cortical bone tissue," *Journal of Biomechanics*, vol. 37, no. 1, pp. 27–35, 2004.
- [118] D. Maggio, E. McCloskey, L. Camilli, S. Cenci, A. Cherubini, J. Kanis, and U. Senin, "Short-term reproducibility of proximal femur bone mineral density in the elderly," *Calcified Tissue International*, vol. 63, no. 4, pp. 296–299, 1998.
- [119] E. S. Orwoll and S. K. Oviatt, "Longitudinal precision of dual-energy X-ray absorptiometry in a multicenter study," *Journal of Bone and Mineral Research*, vol. 6, no. 2, pp. 191–197, 1991.
- [120] G. E.-H. Fuleihan, M. A. Testa, J. E. Angell, N. Porrino, and M. S. Leboff, "Reproducibility of DXA absorptiometry: a model for bone loss estimates," *Journal of Bone and Mineral Research*, vol. 10, no. 7, pp. 1004–1014, 1995.
- [121] R. Patel, G. Blake, J. Rymer, and I. Fogelman, "Long-term precision of DXA scanning assessed over seven years in forty postmenopausal women," *Osteoporosis International*, vol. 11, no. 1, pp. 68–75, 2000.

- [122] T. Nguyen, P. Sambrook, and J. Eisman, "Sources of variability in bone mineral density measurements: implications for study design and analysis of bone loss," *Journal of Bone and Mineral Research*, vol. 12, no. 1, pp. 124–135, 1997.
- [123] W. D. Leslie, "Factors affecting short-term bone density precision assessment and the effect on patient monitoring," *Journal of Bone and Mineral Research*, vol. 23, no. 2, pp. 199–204, 2008.
- [124] T. Pinilla, K. Boardman, M. Bouxsein, E. Myers, and W. Hayes, "Impact direction from a fall influences the failure load of the proximal femur as much as age-related bone loss," *Calcified Tissue International*, vol. 58, no. 4, pp. 231–235, 1996.